

A structural study of hcp and liquid iron under shock compression up to 275 GPa

Saransh Singh^{a,*}, Richard Briggs^a, Martin G. Gorman^a, Lorin X. Benedict^a, Christine J. Wu^a, Amy L. Coleman^a, Federica Coppari^a, Amalia Fernandez-Pañella^b, Christopher McGuire^a, Melissa Sims^c, June K. Wicks^c, Jon H. Eggert^a, Dayne E. Fratanduono^a, Raymond F. Smith^a

^aLawrence Livermore National Laboratory Livermore CA 94550 USA

^bGordon and Betty Moore Foundation Palo Alto CA 94304 USA

^cDepartment of Earth and Planetary Sciences Johns Hopkins University Baltimore Maryland 21218 USA

Abstract

We combine nanosecond laser shock compression with *in-situ* picosecond X-ray diffraction to provide structural data on iron up to 275 GPa. We constrain the extent of hcp-liquid coexistence, the onset of total melt, and the structure within the liquid phase. Our results indicate that iron, under shock compression, melts completely by 258(8) GPa. A coordination number analysis indicates that iron is a simple liquid at these pressure-temperature conditions. We also perform texture analysis between the ambient body-centered-cubic (bcc) α , and the hexagonal-closed-packed (hcp) high-pressure ϵ -phase. We rule out the Rong-Dunlop orientation relationship (OR) between the α and ϵ -phases. However, we cannot distinguish between three other closely related ORs: Burger's, Mao-Bassett-Takahashi, and Potter's OR. The solid-liquid coexistence region is constrained from a melt onset pressure of 225(3) GPa from previously published sound speed measurements and full melt (246.5(1.8)-258(8) GPa) from X-ray diffraction measurements, with an associated latent heat of melting of 362(56) - 542(83) J/g. This value is lower than recently reported theoretical estimates and suggests that the contribution to the earth's geodynamo energy budget from heat release due to freezing of the inner core is smaller than previously thought. Melt pressures for these nanosecond shock experiments are consistent with shock experiments that last for microseconds, indicating that the melt transition occurs rapidly.

1. Introduction

Iron is a cosmochemically abundant element that plays a significant role in terrestrial planetary interiors as the dominant core constituent. The ultra-high pressure properties of iron are essential for interpreting the dynamics and interior structure of the earth and rocky exoplanets (1–3). Within the earth, it is estimated that the solid inner core is comprised of Fe alloyed with ~5-10% of impurities (e.g., Si, S, O, C, H, and Ni) by weight (4). Surrounding the solid inner core is the Fe-rich outer liquid core, which is estimated to have ~8-16% impurity content by weight (4). According to the standard model, convection in the outer core is driven by processes associated with solidification and growth of the inner core. One source is the buoyancy generated by the exclusion of incompatible light elements from the solid. Another is latent heat release from recrystallization. Planetary magnetic fields arising from

convection within the outer liquid Fe-rich cores play an important role in the atmospheric evolution and surface environment of planets (5). There is a strong need to constrain material properties of Fe close to melting at the extreme pressures found within planetary interiors to understand these processes better.

High-pressure static compression studies on Fe have revealed a phase transformation from the ambient body-centered-cubic (bcc) α -phase to a hexagonal-closed packed (hcp) ϵ -phase at 15.3 GPa with an associated 5% volume collapse (6–8). A large (shear-stress dependent) hysteresis of the transition is observed with a midpoint pressure of 12.9 GPa (6–8). The melting of Fe has also been reported as a function of pressure by static compression techniques (1, 7, 9–11), and theoretical calculations (12–14). Under near instantaneous uniaxial shock compression, the $\alpha \rightarrow \epsilon$ phase transformation in polycrystalline Fe samples has been observed, after a period of stress relaxation, to initiate at 12.9 GPa (15–18). At higher pressure, changes in sound speed within mm-thick samples shock compressed over microseconds were used to infer the onset of melt at 225(3) GPa, and

*Corresponding author

Email address: saransh1@llnl.gov (Saransh Singh)

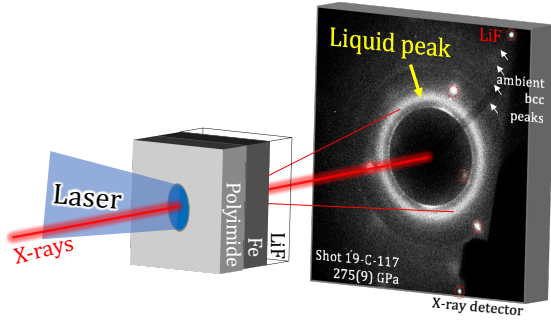


Figure 1: | **Experimental setup.** The target design consists of a polyimide ablator, a 21- μm -thick Fe foil, and a LiF window for velocimetry measurements (21). Raw diffraction data from laser shock compressed Fe at an estimated pressure of 275(9) GPa.

its completion by 260(3) GPa (19). Under nanosecond laser shock-compression of 15- μm thick samples, melt onset was reported to be between 241.5(3)-242.4(2.3) GPa through *in situ* X-ray diffraction (XRD) measurements (20). A further constraint on the high-pressure Fe melt line was reported in a recent laser driven shock-ramp XRD experiments (3).

In the experiments reported here, we employ nanosecond laser shock compression combined with *in situ* picosecond XRD and velocimetry techniques to show that Fe is fully melted along the Hugoniot at 258(8) GPa. We report on the first liquid structural and density measurements of Fe under shock compression. This data, combined with previous sound speed data (19), provides a direct structural determination of the extent of solid-liquid coexistence and a constraint on the latent heat of fusion.

2. Experimental Method

Laser shock compression experiments were conducted at the Dynamic Compression Sector (DCS) beamline of the Advanced Photon Source (APS), located at the Argonne National Laboratory (22). Targets consisted of a polyimide ablator ($\sim 35\text{-}50\ \mu\text{m}$ thickness) glued to high purity 21 μm -thick Fe foil (see Fig. 1). An [100] orientated LiF window was glued to the Fe sample to facilitate measurements of the Fe/LiF particle velocity. A 1-3 μm -thick epoxy held these three layers together. The LiF window is coated with 0.1 μm -thick Ti to enhance reflectivity for velocimetry measurements (VISAR) (21). The full density 99.99% pure Fe foils were supplied by Goodfellow, USA (initial density = 7.874 g/cm³).

A 5 or 10 ns approximately flat-top laser pulse at 351 nm, with energies between 15 and 80 J, was focused within a 580 μm diameter focal spot on the front surface

of the polyimide layer. This setup uniaxially shock-compressed the target assembly and the generated longitudinal stress states in Fe between 25 and 275 GPa. A point-VISAR Doppler velocity interferometer was used to measure the time history of the Fe/LiF interface, $u_p(t)$ (21), and through standard impedance-matching techniques, this allowed a determination of shock pressure in the iron sample. Simultaneously, an X-ray pulse (~ 80 ps) was timed to probe the compressed sample during shock transit within the Fe, which produced an X-ray diffraction pattern recorded in a transmission geometry (Fig. 1), with contributions from the compressed Fe (behind the shock front) and uncompressed Fe (ahead of the shock front). The X-ray energy had a peak of ~ 23.56 keV with a pink beam profile. The experimental geometry is also described in Refs. (22–25).

2.1. X-ray diffraction data processing

CeO₂, and powdered Si calibrants were used to determine the sample to detector distance, beam center, tilt, and rotation. XRD images were azimuthally averaged and analyzed using HEXRD python package (26). First, powder diffraction rings from known standards (CeO₂ and Si) were used for detector calibration. The pink beam profile function detailed in Ref. (27) was used for this step. Next, several intensity corrections were performed to enable accurate density determinations from the diffraction profiles. The intensity corrections included: (i) subtracting the dark counts, (ii) subtracting the ambient Fe pattern for the case of liquid XRD analysis and subtracting LiF single-crystal Laue peaks for all experiments, (iii) correcting for the solid angle subtended by each pixel on the detector (iv) accounting for the polarization factor (for liquid diffraction profiles only) and (v) correcting for the attenuation due to varying path length of the diffracted X-rays. Figure 2 shows representative intensity corrected integrated diffraction profiles for shock-compressed Fe (see also Figs. S12-S14). By increasing the incident drive laser energy to achieve stresses on the Hugoniot between 25 and 275 GPa, a range of XRD profile shapes were observed indicating different Fe structures. Over the stress range studied, Fe exhibits an hcp structure from 25-210 GPa. For the two highest pressure shots (258 and 275 GPa), diffuse scattering around $Q = 3.8\ \text{\AA}^{-1}$ is present in this profile with no evidence of compressed hcp; this is characteristic of the complete melting [$Q = 4\pi\sin(\theta)/\lambda$, where λ is the X-ray wavelength, and θ is the Bragg scattering angle].

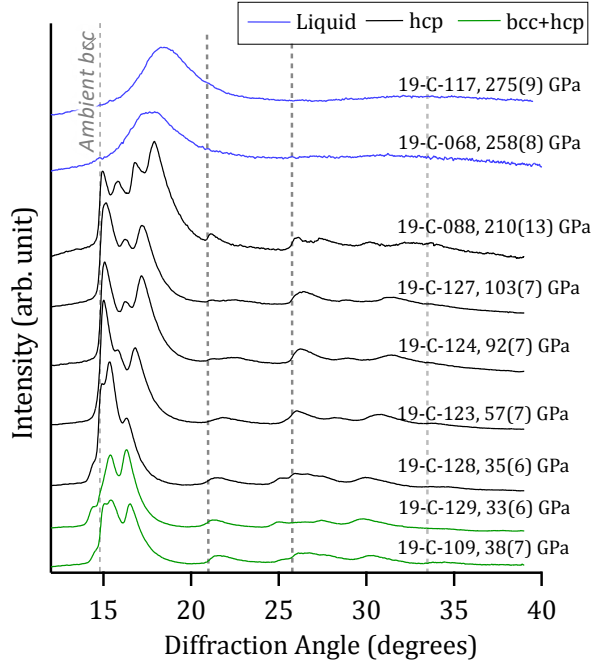


Figure 2: **X-ray diffraction** Azimuthally averaged diffraction data as a function of increasing shock pressure (right axis). The traces are colored coded to depict crystal structure: bcc+hcp (green), hcp (black), and liquid (blue) (see also Figs. S12-S14)

2.2. Stress determination

Standard impedance matching techniques were employed to determine the stress in the Fe layer from the measurement of the Fe/LiF particle velocity, and using U_S-u_p fits (shock velocity-particle velocity, both in km/s) to measure shock compression data for LiF (30) (Eqn. 1) and Fe (Eqn. 2). The Fe/LiF particle velocity was calculated after accounting for the refractive index of LiF under shock compression (30).

$$U_{S,LiF} = 5.215(\pm 0.048) + 1.351(\pm 0.025) \times u_{p,LiF} \quad (1)$$

$$U_{S,Fe} = a + b \times u_{p,Fe} - c \times u_{p,Fe}^2 + d \times u_{p,Fe}^3, \quad (2)$$

where $a = 3.4188 (\pm 0.0539)$, $b = 2.1663 (\pm 0.0823)$, $c = 0.1992 (\pm 0.0369)$, and $d = 0.021219 (\pm 0.00497)$. The uncertainties from impedance matching have contributions from the scatter of EOS data for both Fe (31–52) and LiF (30, 53, 54) and the steadiness of the shock wave as determined in the velocity histories (S5a,c and e). Reported uncertainty in the Hugoniot for Fe and LiF place a *minimum* uncertainty of ± 0.4 GPa for Fe shock stress determination through impedance matching. This value was calculated for $P_{Fe}=250$ GPa, based

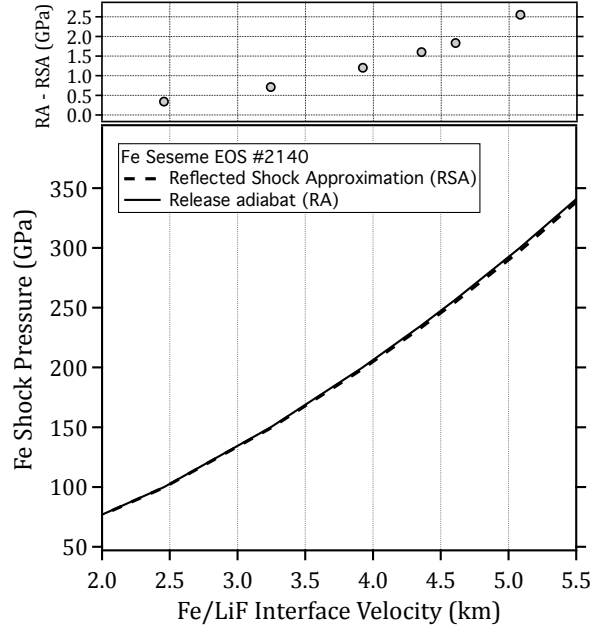


Figure 3: **Pressure determination using Fe-LiF impedance matching.** Using Sesame EOS table 2140 for Fe for a range of assumed LiF u_p values, the main plot shows the calculated Fe pressure calculated through impedance-matching assuming (i) the reflected shock approximation (RSA) and (ii) the release adiabat (RA) approach. In these calculations, the RA path does not include a strength model. While the RA approach is physically correct, the RSA is often used in impedance matching because it simplifies the analysis, as one needs only the Hugoniot data to perform the analysis. In contrast, the RA approach relies on a theoretical model (28, 29). The upper plot represents underestimating of the calculated Fe pressure from the RSA approach as a function of increasing pressure. This offset has been accounted for in our pressure estimate.

on fits to Hugoniot data with $1-\sigma$ confidence bands. Confidence bands rely only on the fit coefficients and the estimated uncertainties in the coefficients. This value represents a systematic uncertainty and is combined with estimated random uncertainties (described below) to give the total pressure uncertainty values reported in Table S1. While the use of reflected Hugoniot is a standard approximation for the pressure determination through impedance matching (28, 29), we note that at high pressure, the use of a release adiabat is needed (Fig. 3). In our analysis, we initially conducted impedance matching using the reflected shock approximations and then made an additional correction based on the trend in Fig. 3, upper.

The measured Fe/LiF particle velocity profiles, shown in Figure S5, are characterized by an initial shock followed by a time-dependent distribution of velocity states. The stress in the sample (as reported in Table S1) is calculated through impedance matching while consid-

ering the velocity distribution after the initial shock (see Fig. 4b). The calculated random uncertainty in stress is a contribution of the following: (i) the standard distribution of velocity states above the initial shock, and (ii) the accuracy with which fringe shifts can be measured in the point-VISAR system, taken here as 0.024 km/s (2% of a fringe shift (21)). Other contributors to stress uncertainty that is not explicitly treated relate to uncertainties in the refractive index of LiF (30), uncertainties in the timing of the X-ray probe with respect to the VISAR, and uncertainties in the measurements of sample thickness. In addition, the point VISAR system integrates spatially and therefore does not provide any information on the distribution of stress states which may arise due to non-planarities within the drive (as in Ref. (24)). Moreover, in the case of a detected Fe/LiF velocity profile which is characterized by an initial shock followed by an increase in velocity, there is a progressive increase in shock strength throughout the sample as late-time characteristics catch up and reinforce, to some extent, the shock front during transit. To account for these additional uncertainties, we increase our total pressure uncertainties by an additional ± 5 GPa. We note that our pressure uncertainties are similar to Ref. (24) but are significantly higher than reported in Refs. (20, 55). The high-pressure constraint for solid-liquid coexistence in Fe is shot 19-C-068, which is the lowest pressure observation of liquid only. The calculated pressure for this shot based on impedance matching as described above is 258(8) GPa.

As an additional check on the pressure and pressure distribution within the sample during the X-ray probe time, the pressure history in Fe is also determined by simulating the experimental conditions with a 1D hydrocode, HYADES (56), which calculates the hydrodynamic flow of pressure waves through the target assembly in time (t) and Lagrangian space (h) (Fig. 4a). The inputs to the hydrocode are the thicknesses of each of the constituent layers of the target, including the measured epoxy layer thicknesses (~ 1 -3- μ m), an equation-of-state (EOS) description of each of the materials within the target, and laser intensity as a function of time, $I_{\text{Laser}}(t)$. Based on experience over hundreds of shots, we find that pressure (GPa) in the polyimide ablator scales approximately as $4.65 \times I_{\text{Laser}}^{0.8}$, with $I_{\text{Laser}}(t)$ (PW/m²) calculated from measurements of laser power divided by an estimate of the laser spot size (Fig. S4). A series of forward calculations were run with iterative adjustments of $I_{\text{Laser}}(t)$ (few % level) until convergence was reached between the calculated $u_{p,\text{LiF}}(t)$ and the measured $u_{p,\text{LiF}}(t)$ curves (Fig. 4b). Once achieved, the calculated $P(h,t)$, at the X-ray probe time, is used

to estimate the volume-integrated pressure and pressure distribution in the Fe sample. This method of pressure determination explicitly accounts for any temporal non-steadiness in the compression wave. The results of the hydrocode simulations in Fig. 4 are for s19-C-068, which in our experiments represents the first liquid-only shot (the upper-pressure constraint of the solid-liquid coexistence). The determined pressure in the Fe sample from the hydrocode simulations is 255.0(2.2) GPa, which is in agreement with the impedance matching approach (258(8) GPa) described above.

3. Results

3.1. Liquid structure measurements

The high flux of the X-ray source at DCS coupled with angular coverage up to almost 8 \AA^{-1} permits quantitative analysis of liquid density recorded using ps X-ray diffraction. Due to the non-monochromatic “pink” X-ray beam, the raw liquid diffraction intensities are artificially shifted to higher Q (58). The corrections outlined in Ref. (59) were applied to account for this artificial shift and derive quantitative densities. This method has already been applied to other simple metallic systems such as Ag, Sn, and Cu and shows good agreement with the Hugoniot pressure-density relationship (24, 25, 59). Figures 5a,b presents the structure factor, $S(Q)$, and the corresponding radial distribution functions, $g(r)$ of the two shots with complete melting (solid black lines). The lowest and highest pressure liquid structure data presented in Ref. (10) have also been shown (markers and dashed lines). That data was collected using a laser-heated diamond anvil cell apparatus up to a maximum pressure of 116 GPa, providing the density of liquid iron along several isotherms that lie close to the melting temperature (10). The $S(Q)$ and $g(r)$ follow the expected behavior of shifting to higher Q and lower r . The coordination number (CN) was determined by integrating the area under the first peak in the radial distribution function. Two different integration schemes were followed for determining the CN: (i) twice the area up to the peak and (ii) the area up to the first minimum when plotting $4\pi n r^2 g(r)$ against r (n is the number density). We find that the coordination number at 258(8) and 275(9) GPa are ~ 11.7 and 12.2 , respectively, using the first method, and 12.7 and 12.9 using the second method. Either method shows simple liquid behavior.

Figure 6 shows our data in pressure-density space, color-coded with measured phase (blue: bcc, red: hcp, cyan: liquid), and plotted against other shock, ramp,

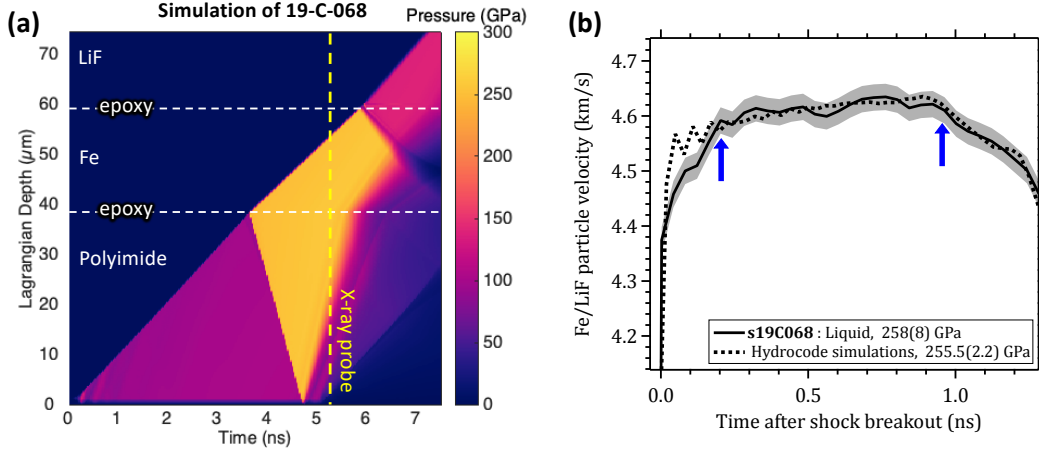


Figure 4: | **Hyades simulation of shot 19-C-068.** **a.** Calculated map of pressure distribution throughout the target package, where the horizontal dashed lines indicate material boundaries in Lagrangian coordinates. For this shot, the 80 ps X-ray pulse probed the sample 0.7 ns before shock breakout into the LiF window. The resultant X-ray diffraction pattern is volume integrated and therefore includes a scattering contribution from the ambient material ahead of the shock front as well as the shocked material (behind the shock front). In this simulation, Fe EOS table #2150 from Ref. (57) was used. **b.** Agreement between measured (solid) with calculated $u_{p, \text{LiF}}(t)$ (dashed). Using the impedance matching approach for determining pressure, we obtain a value of 258(8) GPa. For this estimate, we consider the velocity distribution over the period between the two blue arrows. These peak velocity values are most closely associated with the location of the peak of the diffraction data, which is used to calculate density. During the X-ray probe period, the hydrocode simulations calculate a value of 255.5(2.2) GPa, consistent with the impedance matching estimates.

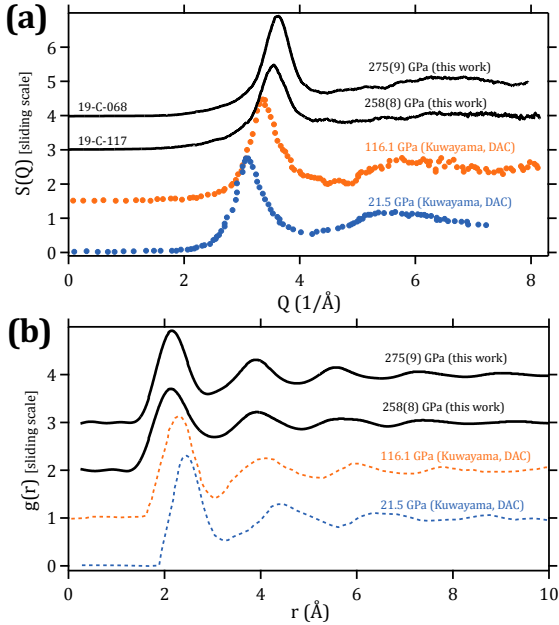


Figure 5: | **Liquid structure measurements.** **a.** Liquid structure factor (solid lines) and **b.** corresponding radial distribution function (solid lines) for dynamically compressed Fe at 258(8) GPa (s19-C-068) and 275(9) GPa (s19-C-117). Also shown is liquid XRD data taken at lower pressure under laser-heated static compression (markers and dashed lines) (10).

and static compression datasets. Also plotted is the P - ρ curve estimated from the Preliminary Reference Earth

Model (PREM) (65) for the outer liquid and solid inner core (IC). At 180 GPa, where the P - T conditions along the Fe Hugoniot (63) are comparable to those found within the outer liquid core (~ 180 GPa, ~ 4080 K, see Fig. 7), there is a 10.1% difference in the density. The lower density of the Fe-rich outer core is expected due to the inclusion of 2.7-11.5% by weight of low-Z impurities (4). The inset to Fig. 6 shows the magnified view of the structural measurements from this study (solid horizontal line). The green hatched region shows the coexistence region determined using sound speed measurements from a previous study (19). A dashed horizontal line also shows the melt onset pressure from a recent XRD study in Ref. (20) at 241.5(3) GPa. Based on the XRD study presented in this work (melt completion) and in the XRD study of Ref. (20) (melt onset), the liquid-solid coexistence lies between 241.5(3)-258(8) GPa. This coexistence is smaller than the 225(3)-260(3) GPa range inferred by Nguyen and Holmes (19) from experiments that measure changes in sound speed as a function of pressure for microsecond shock compression of mm-thick Fe samples (see Supplementary Materials Fig. S1) – although a reanalysis of this data is planned based on a reevaluation of uncertainty analysis (66).

One contributing factor for the discrepancy in melt onset pressures between the two experimental approaches (XRD and sound speed) *may* lies in a lower

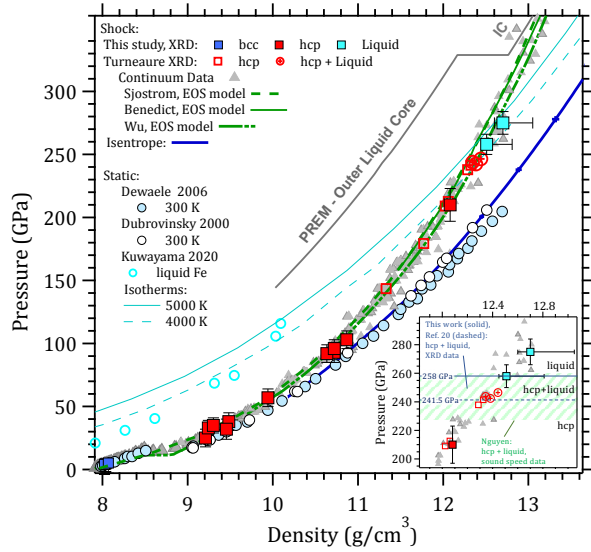


Figure 6: **Pressure versus density.** P - ρ data from this study (bcc - blue squares, hcp - red squares, and liquid - cyan squares), and a previous XRD study (20) (hcp - red open squares, hcp+liquid - red crossed circles). Previously published Hugoniot (2) (gray triangles), and 300 K static data (10, 60, 61) (blue and white filled circles) are also shown, as well as an isentrope determined from laser ramp-compression experiments (blue curve) (2). High-temperature liquid static data is shown by the open cyan circle along with calculated 4000 K and 5000 K isotherms (10). Three Hugoniot models are also shown (green curves) (62–64). (Inset) A magnified view shows agreement for melt completion pressures along the Hugoniot between our XRD data and previous sound speed measurements (19). However, previous XRD data (20) and sound speed measurements (19) disagree on the melt onset pressures along the Hugoniot. These combined XRD studies constrain the hcp+liquid coexistence along the Hugoniot between 241.5(3)–258(8) GPa, whereas it is 225(3)–258(8) GPa using the combined sound speed measurements and XRD data from this study.

sensitivity of XRD in detecting the weak diffuse signal of the incipient liquid phase. The sound speed technique is expected to be sensitive to the onset of melting. Both the shear and bulk moduli contribute to the sound velocity in a solid. In contrast, the shear modulus $\rightarrow 0$ in a liquid, resulting in a sharp decrease in sound velocity on crossing the melt curve (19) (see Fig. S1). This is expected to be more sensitive than XRD measurements to the onset of small volumes of liquid (see Supplementary Methods). However the sound speed measurements are less constraining for the completion of the melt. In the case of Fe there is a sparsity of data (no data between 247 and 260 GPa, see Fig. 7c). The completion of melt, however, is well constrained through XRD as small volumes of a textured solid are easily observed. We note that while the lowest pressure liquid-only data presented here is at 258(8) GPa, the pressure for melt completion is constrained by this value and the observation of high-pressure hcp from a previous XRD study

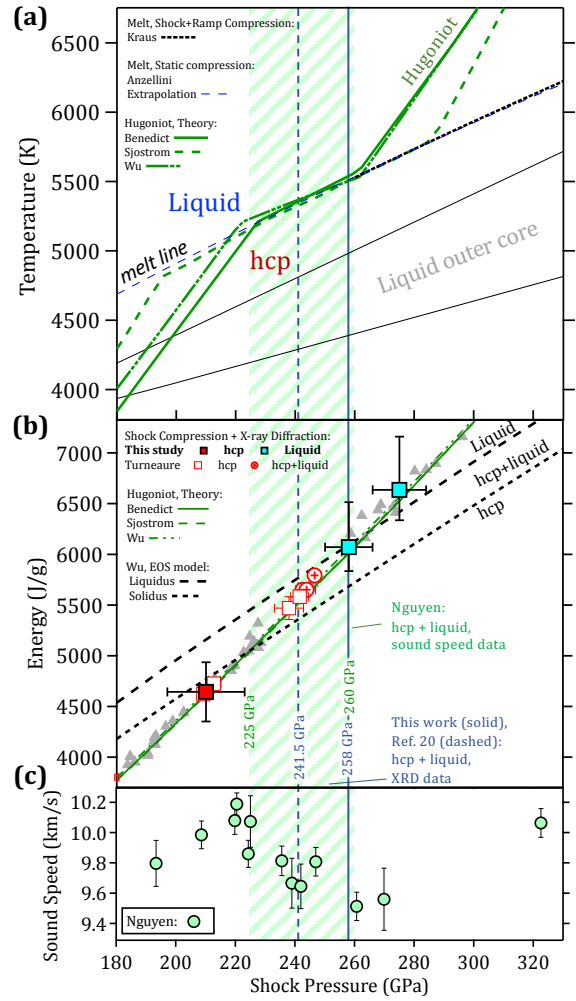


Figure 7: **Fe pressure-temperature phase map.** **a.** High P - T region of the Fe phase map, which shows the stability regions for the ϵ -hcp, and the liquid phases. The melt line is constrained by static (1), and nanosecond timescale shock+ramp compression experimental data (3). Three theoretical bounds on the Hugoniot are represented by the solid (63) and dashed (64), and dashed-dotted green curves (62). The extent of solid-liquid coexistence in the Benedict (63) and Wu (62) models are set by the measured changes in sound speed under shock compression of Nguyen and Holmes (19) (see **c.** and Fig. S1), which are inferred in that study to reflect the onset and completion of melt. Our XRD data point for melt completion at 258(8) GPa is consistent with previous sound speed determinations of solid-liquid coexistence (green band). However, the XRD data point for melt onset reported in (20) at 241.5(3) GPa is inconsistent with previous measurements. This may be related to the insensitivity of X-ray diffraction to measure small volumes of liquid (see Supplementary Materials). Also shown is the range of possible temperatures for the earth's outer core (65). A more inclusive representation of experimental and theoretical studies of Fe in P - T space is shown in Fig. S2. **b.** Energy vs. pressure plot, which shows our shock-compression data, previous Hugoniot data ((2), grey triangles), theoretical predictions for the Hugoniot (62–64), and solidus and liquidus curves (derived from EOS in Ref. (62)). **c.** Sound speed data from Ref. (19).

(20), to be in the range 246.5(1.8)-258(8) GPa.

The consistency in the pressures for melt completion between experiments with shock compression durations which differ by over three orders of magnitude is consistent with a lack of time-dependence in the melt of Fe. This is in contrast to the reported strong time-dependence reported for the low-pressure $\alpha \rightarrow \epsilon$ phase transformation (67).

Figure 7a shows the pressure-temperature (P - T) phase map of Fe in the vicinity of the melt line with three recent Hugoniot models (62–64). These models were constructed to cross the melt line in agreement with the extrapolated melt of the static compression study of Anzellini *et al.* (1) and the dynamic ns-compression work of Kraus *et al.* (3). The pressure extent of the solid-liquid coexistence for the Wu *et al.*, and Benedict *et al.* Hugoniots were set to agree with the 225(3)-260(3) GPa range inferred from sound speed measurements from Nguyen and Holmes (19) (see also Supplementary Materials Fig. S1).

The internal energy of the solidus and liquidus curves from the Wu EOS model is plotted in Fig. 7b (62). By using the Rankine-Hugoniot equations, based on conservation of energy, $E = \frac{1}{2} P((\rho - \rho_0)/\rho \rho_0)$ (68), where P is the experimentally-determined shock pressure, ρ is the density from X-ray diffraction measurements, and ρ_0 is the initial density (7.874 g/cm³), we can compare our measured Hugoniot data with the calculated Hugoniot and melting curve, and provide a valuable description of the Fe phase diagram in pressure-energy space (Fig. 7b).

3.2. $\alpha \rightarrow \epsilon$ solid-solid phase transition

Iron undergoes bcc α to hcp ϵ phase transformation around 13 GPa (69). The geometrical mapping from the bcc to the hcp phase has been an active area of study for decades with several phase transition mechanisms proposed in the literature (70–73). In our study, XRD data provides information on microstructural changes in Fe across the $\alpha \rightarrow \epsilon$ phase boundary. A forward diffraction and texture analysis approach is employed to relate measured azimuthal (ϕ) diffraction intensities with those predicted from mechanistic transformation pathway models.

Texture measurement using X-ray diffraction usually involves measuring pole figures and inverting the pole figures to obtain the full orientation distribution function. These measurements are routine for static compression experiments to measure the orientation relationship between ambient and high-pressure phases. However, due to the *ns* timescales of shock compression experiments, the measurement of the complete pole

figure is not feasible in our measurements. Only a single ring of the complete pole figure is measured, which makes crystallographic texture determination using pole figure inversion ill-conditioned. Therefore, we employ a forward diffraction model to measure the orientation relationship (OR). Given all experiment parameters, the model computes the intensity distribution in $2\theta - \phi$ space. These include:

1. The crystal structure, lattice parameters, and phase fraction of the ambient and high-pressure phase, including the Debye-Waller factors. This information is used to compute the powder diffraction intensity in 2θ .
2. Crystallographic texture of the ambient and high-pressure phase. This information modulates the powder intensity in the ϕ direction.
3. X-ray source specification such as polarization and meaningful peak shapes for the X-ray source. In our case, we use the “pink” beam function, which is a convolution of back-to-back exponential functions with a Gaussian and Lorentzian function described in Ref. (27).

The crystallographic texture is represented using a finite element representation of the Rodrigues space fundamental zone (74–76).

The samples used in lower pressure shots ($P < 60$ GPa, see Table S1) were highly textured and had significant intensity variation in the azimuthal direction of the Debye-Scherrer rings (see Supp. Mat. Fig. S11a). Upon compression, the high-pressure hcp ϵ -phase had a repeatable intensity distribution with the ambient pressure texture. The texture is used to compute the complete pole figures using the methodology described in Ref. (74). The pole figures computed for the ambient bcc phase using the forward model are shown in Fig. S6. Only a single ring of the entire pole figure is measured in the experiment, shown by the red dotted circle. The intensity variation along this ring modulates the powder diffraction intensity for each diffraction line. The resulting diffraction pattern after applying the azimuthal modulation is shown in Figs. 9c, S11a.

A static compression study of single crystal Fe unambiguously demonstrated that the OR between the single crystal α and high-pressure ϵ -phase was the Burger’s OR $[(110)_\alpha || (0001)_\epsilon]$ and $[1\bar{1}1]_\alpha || [11\bar{2}0]_\epsilon$ (77). All 12 orientation variants predicted by Burger’s mechanism were observed in the study. However, the mechanism during dynamic compression experiments is still unknown. An alternative mechanism has been proposed in Ref. (71) resulting in the OR $(110)_\alpha || (0001)_\epsilon$ and

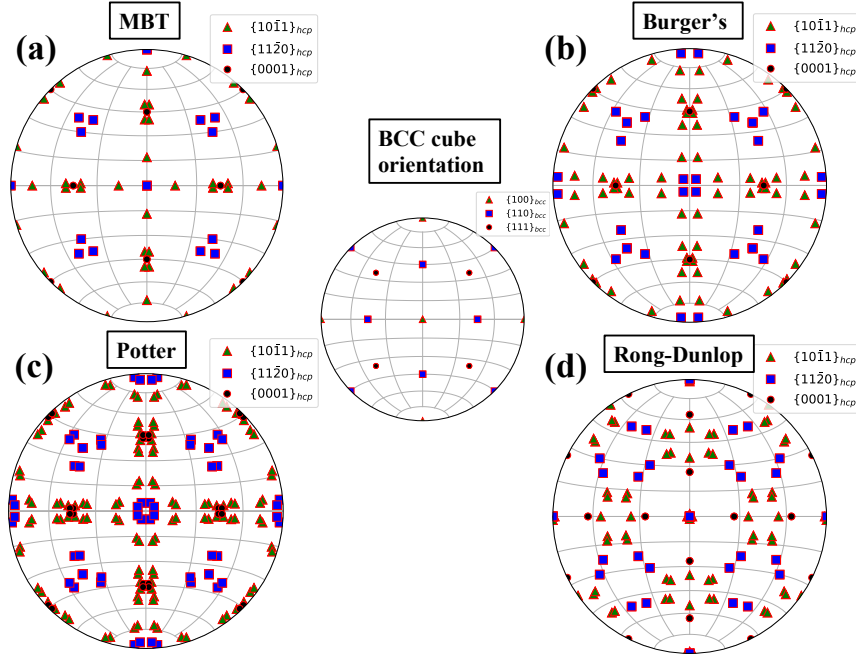


Figure 8: **Pole figures for different mechanisms** Pole figures for some low index planes ambient cubic BCC phase in the cube orientation and high pressure hexagonal closed packed phase as a result of the different phase transition mechanisms: (a) Mao-Bassett-Takahashi OR given by the $(110)_{\text{bcc}} \parallel (0001)_{\text{hcp}}$ and $[001]_{\text{bcc}} \parallel [2\bar{1}\bar{1}0]_{\text{hcp}}$ (6 variants), (b) Burger's OR given by $(110)_{\text{bcc}} \parallel (0001)_{\text{hcp}}$ and $[1\bar{1}1]_{\text{bcc}} \parallel [11\bar{2}0]_{\text{hcp}}$ (12 variants), (c) Potter OR given by $(110)_{\text{bcc}} \parallel (1\bar{1}01)_{\text{hcp}}$ and $[1\bar{1}1]_{\text{bcc}} \parallel [11\bar{2}0]_{\text{hcp}}$ (24 variants) and (d) Rong-Dunlop OR given by $(021)_{\text{bcc}} \parallel (0001)_{\text{hcp}}$ and $[100]_{\text{bcc}} \parallel [11\bar{2}0]_{\text{hcp}}$ (12 variants).

$[001]_{\alpha} \parallel [2\bar{1}\bar{1}0]_{\epsilon}$. We refer to this as the Mao-Bassett-Takahashi (MBT) OR. The MBT mechanism results in 6 orientation variants that can form from a single α -phase grain, half the number of variants formed in the Burger's OR (70). We also considered experimentally observed bcc-hcp ORs for other material systems (72, 73). The distribution of some low-index ϵ -phase planes formed as a result of these ORs are shown in Fig. 8a-d. Three of the four ORs produce very similar distributions of the crystallographic planes. The $\{0001\}_{\epsilon}$ planes formed by Burger's and MBT OR are identically distributed, while the angular separation of the $\{11\bar{2}0\}_{\epsilon}$ plane is only 5.26° . The OR observed by Potter (73) produces twice the number of variants as the Burger's OR, with each pair of the variants separated by $\sim 2^{\circ}$ to the Burger's variant. The full ORs are listed in Table 1.

The pole figure of some low-index ϵ -phase planes formed due to these ORs is shown in Fig. 8. Note that these pole figures are for the cube orientation of the ambient bcc phase such that $(001)_{\alpha} \parallel \mathbf{z}_{\text{lab}}$ and $[100]_{\epsilon} \parallel \mathbf{x}_{\text{lab}}$. Since the ambient α -phase has a pole figure different from the cube orientation as shown in Fig. S6, the pole figures for the high-pressure ϵ -phase formed as a re-

sult of the different ORs listed in Table. 1 is calculated by applying the starting orientation of the ambient bcc phase to the pole figures shown in Fig. 8. The calculated pole figures for the high-pressure hcp phase following the Burger's, Mao-Bassett-Takahashi, Potter, and Rong-Dunlop orientation relationships are shown in Figs. S7, S8, S9, S10 respectively, and the resulting diffraction pattern are shown in Figs. 9d, S11b-d respectively.

Fig. 9a shows the results of the forward calculation for shot 19-C-122 [25(7) GPa], with experimental data shown in Fig. 9b. The lattice parameters were determined by performing a LeBail fit to the 1-D line-outs (see Figs. S12, S13, S14). Here, Burger's OR was applied to the ambient phase texture to obtain the ϵ -phase texture, with good agreement to the experimentally measured XRD pattern. The diffraction signal consists of ambient α - (20%) and high-pressure ϵ -phase (80%), with a complete transformation to all variants of the ϵ -phase.

The results of the forward model are compared with the experimental measurements by comparing the azimuthal variation of some lower-angle diffraction lines. While we rule out the Rong-Dunlop OR (72) based on this calculation, our data are unable to distin-

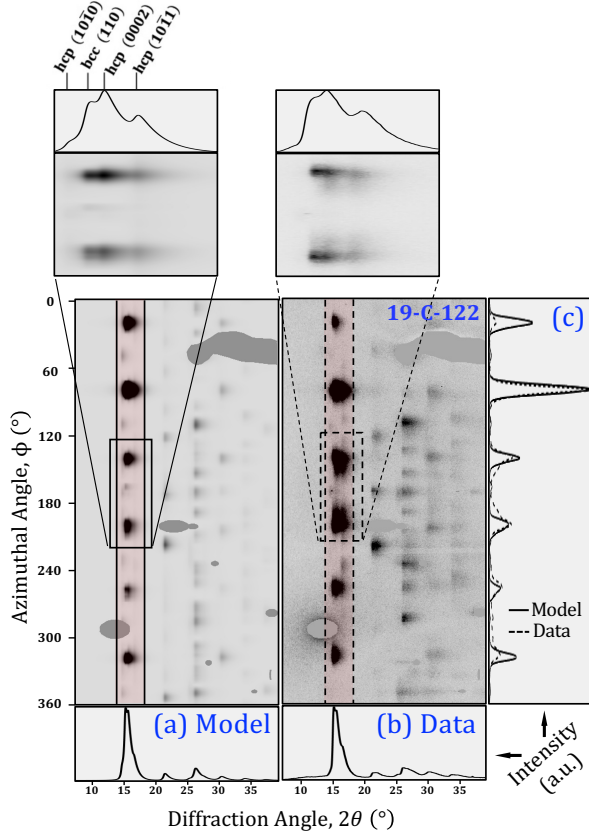


Figure 9: | **Texture as a result of Burger's OR.** **a.** Forward model simulation of XRD pattern and **b.** experimentally measured XRD pattern for Fe shock compressed to 25(7) GPa (shot 19-C-122). The diffraction data is a combination of the ambient α -phase (ahead of the shock wave) and the compressed ϵ -phase (e.g., see top panels). The orientation distribution of the high-pressure phase was determined by applying Burger's OR to the ambient α -phase orientation distribution. Averaged profiles in 2θ are shown in lower panels, and profiles averaged in ϕ over the regions of interest defined by the solid (model), and dashed boxes (data) are shown in **c**.

guish between the ORs from Burger (70), Mao-Bassett-Takahashi (78), or the Potter mechanisms (73). High-quality single crystal samples having a small orientation spread, together with highly monochromatic X-rays need to be employed to unambiguously identify the phase transition OR for iron during dynamic compression.

4. Discussion

Latent heat release (ΔH_m) associated with freezing at the Earth's inner core boundary (ICB) is regarded as one of the primary drivers ($\sim 20\%$ of total energy contribution (79)) of convection currents in the outer core. This value has not been directly constrained experimentally at ICB conditions, and therefore models describing the

core dynamics rely on theoretical calculations of ΔH_m (80–82). The entropy of fusion ($\Delta S_m = \Delta H_m/T_m$) for simple systems is expected to approach the gas constant, R asymptotically at high pressure (83), commonly referred to as Richard's rule. Since our liquid structure measurement of Fe on the Hugoniot demonstrate that Fe remains a simple liquid at these conditions, such behavior is expected.

Experimentally, this value can be constrained at the high P - T conditions accessed along the Hugoniot by a measure of the extent of solid-liquid coexistence and knowledge of the equation of state of Fe (see Supplementary Materials). The measurement of melt completion in this study together with previous measurements of melt onset (19), can be used to constrain the latent heat of fusion at 258 GPa to 542(83) J/g, equivalent to the entropy of fusion, $\Delta S_m = 0.66R$ (see Supp. Mat. Sec. S1). This value is significantly lower than the expected value of R , and approximately half of three recent theory predictions at this pressure (81), and suggests that the energy contribution to the geodynamo budget due to the freezing of Fe is smaller than previously thought. We also note that the latent heat at the same pressure derived from the Fe EOS model of Wu *et al.* (62) is 666.9 J/g, corresponding to $\Delta S_m = 0.82R$. If the previous XRD measurement of 241.5(3) GPa (20) is used to constrain the melt onset, then a latent heat of fusion of 243.4(77) J/g is obtained. This corresponds to $\Delta S_m = 0.3R$, a value much lower than expected from Richard's rule (83), especially for a simple liquid system such as Fe (see Fig. 5a,b). If this value is true, it likely points to new physics in liquid Fe at planetary interior conditions.

If the latent heat of fusion at the inner core boundary pressure (330 GPa) changes negligibly due to higher pressure and a small amount of impurities, the total power output due to the solidification of the inner core can be computed. This quantity is the ratio of the heat generated due to the solidification and the time over which the solidification occurred. The heat generated due to solidification is given by the product of ΔH_m of pure iron and the mass of the inner core (1.1×10^{23} Kg (84)). The latest estimates for the age of Earth's inner core range between 0.565–4 billion years (85–88). This results in power output, when considering our estimates of latent heat, of 0.47(7) – 3.35(5) TW, which is lower than previous estimates (89). This discrepancy suggests the importance of compositional convection and/or radioactive heating (90, 91) in maintaining the Earth's geodynamo.

The depression in the melting point over pure material can be estimated, assuming an ideal mixing model

Table 1: Commonly observed orientation relationships between bcc and hcp phases

Authors	Details	$(hkl)_\alpha \parallel (hkl)_\epsilon$ $[uvw]_\alpha \parallel [uvw]_\epsilon$
Burger's (70) (1934)	Experimental X-ray diffraction study on the orientation relationship between the hcp α - and bcc β -phase in Zr.	$(110)_\alpha \parallel (0001)_\epsilon$ $[\bar{1}\bar{1}1]_\alpha \parallel [11\bar{2}0]_\epsilon$
Mao-Bassett-Takahashi (78) (1967)	Experimental X-ray diffraction study on the orientation relationship between the ambient α -phase and high-pressure ϵ -phase in Fe	$(110)_\alpha \parallel (0001)_\epsilon$ $[001]_\alpha \parallel [2\bar{1}\bar{1}0]_\epsilon$
Potter (73) (1973)	Experimental study on orientation relationship between bcc α -phase in Vanadium-Nitrogen system and hcp V_3N precipitate using transmission electron microscopy	$(110)_\alpha \parallel (1\bar{1}01)_\epsilon$ $[\bar{1}\bar{1}1]_\alpha \parallel [11\bar{2}0]_\epsilon$
Rong-Dunlop (72) (1973)	Experimental study on orientation relationship between bcc α -ferrite and hcp M_2C ($M = Cr, Mo, Fe$) precipitates in ASP23 high strength steel using a transmission electron microscope	$(021)_\alpha \parallel (0001)_\epsilon$ $[100]_\alpha \parallel [11\bar{2}0]_\epsilon$

and thermodynamic equilibrium between pure solid and liquid with impurities. It is given by (89)

$$\log(1 - \chi_s) = \frac{-\Delta H_m}{R} \left(\frac{1}{T} - \frac{1}{T^*} \right). \quad (3)$$

Here, χ_s is the mole fraction of impurities, R is the gas constant, T^* is the melt temperature of the pure material, and T is the melt temperature in the presence of impurities. For the same level of impurity, a smaller latent heat will result in a larger drop in the melting temperature. It is estimated that the liquid outer core contains approximately 2.7 – 11.5% light impurities by weight (4). The melting temperature at the inner core boundary (ICB; $P = 330$ GPa) using the melt curve in Ref. (3) is approximately 6220 K. Using the estimate of the latent heat in this study, the temperature of outer core side of ICB is constrained to a range of 3600 – 5650 K. We note that the upper bound of this range is more accurate than the lower bound as Eqn. 3 holds better for dilute solutions, i.e., small χ_s .

In a shock compression study of single crystal iron along the $[100]$ direction (92), the authors reported formation of polycrystalline hcp ϵ -phase with the grain size between 2 and 15 nm, with the conclusion that "single-crystal iron becomes nanocrystalline in shock transforming from α to ϵ phase." While our *in-situ* diffraction results do not disagree with these results, it presents a more nuanced picture of the grain refinement. The overall texture of the ambient α and the high-pressure ϵ -phase is explained well by a unimodal orientation distribution. This is akin to a Gaussian distribution around specific orientations. The full width at half-

max (fwhm) for the ambient and high-pressure phase that gives the best agreement with experimental data is $\sim 2^\circ$ and $\sim 4^\circ$, respectively. While each grain retains the mean orientation predicted by the phase transformation mechanism, the orientation distribution within each grain points to microstructure refinement with the possibility that each "sub-grain" with that grain is nm-sized. There is no large-scale grain refinement to result in an almost powder-like diffraction pattern from the high-pressure ϵ -phase.

5. Conclusions

In conclusion, we present a detailed structural study of Fe under shock compression from 25 to 275 GPa. Liquid scattering data were analyzed to obtain the radial distribution factor and density on the shock Hugoniot (59). The upper bound shock pressure for complete melt was found to be 258(8) GPa. A forward diffraction model is used to perform texture analysis of the ambient bcc α -phase and high-pressure hcp ϵ -phase. Some commonly observed orientation relationships between bcc and hcp phases are tested for consistency with our diffraction data. We are able to rule out the Rong-Dunlop OR. However, our data can not distinguish between Burger's, MBT, and Potter's orientation relationship. Our XRD data, along with previous melt onset determination using sound speed measurements (19), suggest an hcp-liquid coexistence along the Hugoniot (225(3)-258(8) GPa). Our data is consistent with an internal energy change due to melting of 542(83) J/g at 258(8) GPa, which is approximately half of recent theoretical studies, and a value that suggests that the energy

contribution to the geodynamo budget due to freezing of Fe at the inner core boundary is smaller than previously thought. The small latent heat also suggests a larger decrease in the melting temperature in the presence of impurities than previously estimated.

Acknowledgements

We would like to thank Carol Ann Davis for her help in preparing the Fe targets. Paulo Rigg, Pinaki Das, Ray Gunawidjaja, Yuelin Li, Adam Schuman, Nicholas Sinclair, Xiaoming Wang, and Jun Zhang at the Dynamic Compression Sector are gratefully acknowledged for their expert assistance with the laser experiments. We thank Yoshi Toyoda for his assistance with VISAR measurements during the laser experiments, and Richard Kraus for helpful discussions on pressure uncertainties. This work was performed under the auspices of the US Department of Energy by Lawrence Livermore National Laboratory under contract number DE-AC52-07NA27344. This publication is based upon work performed at the Dynamic Compression Sector, which is operated by Washington State University under the US Department of Energy (DOE)/National Nuclear Security Administration under Award No. DE-NA0003957. This research used resources from the Advanced Photon Source, a DOE Office of Science User Facility operated for the DOE Office of Science by Argonne National Laboratory under Contract No. DE-AC02-06CH11357.

References

- [1] S. Anzellini, A. Dewaele, M. Mezouar, P. Loubeyre, G. Morard, *Science* **340**, 464 (2013).
- [2] R. F. Smith *et al.*, *Nature Astronomy* **2**(6), 452 (2018).
- [3] R. G. Kraus *et al.*, *Science* **375**(6577), 202 (2022).
- [4] K. Hirose, B. Wood, L. Vočadlo, *Nature Reviews Earth & Environment* **2**(9), 645 09 2021.
- [5] B. J. Foley and P. E. Driscoll, *Geochemistry, Geophysics, Geosystems* **17**, 1885 (2016).
- [6] N. V. Barge and R. Boehler, *High Pressure Research* **6**(2), 133 (1990).
- [7] R. Boehler, N. Von Bargen, A. Chopelas, *Journal of Geophysical Research: Solid Earth* **95**(B13), 21731 (1990).
- [8] R. Taylor, M. Pasternak, R. Jeanloz, *Journal of applied physics* **69**(8), 6126 (1991).
- [9] R. Sinmyo, K. Hirose, Y. Ohishi, *Earth and Planetary Science Letters* **510**, 45 (2019).
- [10] Y. Kuwayama *et al.*, *Phys. Rev. Lett.* **124**(16), 165701 (2020).
- [11] R. Boehler, *Nature* **363**(6429), 534 (1993).
- [12] A. B. Belonoshko, R. Ahuja, B. Johansson, *Physical Review Letters* **84**(16), 3638 (2000).
- [13] D. Alfe, *Physical Review B* **79**(6), 060101 (2009).
- [14] D. C. Swift, T. Lockard, R. F. Smith, C. J. Wu, L. X. Benedict, *Physical Review Research* **2**(2), 023034 (2020).
- [15] D. Bancroft, E. L. Peterson, S. Minshall, *Journal of Applied Physics* **27**(3), 291 (1956).
- [16] B. J. Jensen, G. T. Gray, R. S. Hixson, *J. Appl. Phys.* **105**(10), 103502 (2009).
- [17] L. M. Barker and R. E. Hollenbach, *J. Appl. Phys.* **45**, 4872 (1974).
- [18] L. Barker, *Journal of Applied Physics* **46**(6), 2544 (1975).
- [19] J. H. Nguyen and N. C. Holmes, *Nature* **427**, 339 (2004).
- [20] S. J. Turneaure, S. M. Sharma, Y. M. Gupta, *Phys. Rev. Lett.* **125**, 215702 11 2020.
- [21] D. H. Dolan, Technical report Sandia National Laboratories (SNL), Albuquerque, NM, and Livermore, CA (2006).
- [22] X. Wang *et al.*, *Review of Scientific Instruments* **90**(5), 053901 (2019).
- [23] R. Briggs *et al.*, *Physical review letters* **123**(4), 045701 (2019).
- [24] A. L. Coleman *et al.*, *Journal of Applied Physics* **131**, 015901 1 2022.
- [25] M. Sims *et al.*, *Journal of Applied Physics* **132**(7), 075902 (2022).
- [26] <https://github.com/HEXRD/hexrd>, LLNL-CODE-819716.
- [27] R. B. Von Dreele, S. M. Clarke, J. P. S. Walsh, *Journal of Applied Crystallography* **54**(1), 3 2 2021.
- [28] P. M. Celliers, G. W. Collins, D. G. Hicks, J. H. Eggert, *Journal of Applied Physics* **98**(11), 113529 (2005).
- [29] G. I. Kerley, (2013).
- [30] P. Rigg, M. Knudson, R. Scharff, R. Hixson, *Journal of Applied Physics* **116**(3), 033515 (2014).
- [31] J. M. Walsh, M. H. Rice, R. G. McQueen, F. L. Yarger, *Physical Review* **108**, 196 (1957).
- [32] L. V. Al'tshuler, K. K. Krupnikov, B. N. Ledenev, V. I. Zhuchikhin, M. I. Brazhnik, *Zhur. Eksptl'. i Teoret. Fiz.* **34** (1958).
- [33] L. V. Al'tshuler, A. A. Bakanova, R. F. Trunin, *Sov. Phys. JETP* **15**, 65 (1962).
- [34] L. V. Al'tshuler, B. N. Moiseev, L. V. Popov, G. V. Simakov, R. F. Trunin, *Sov. Phys. JETP* **27**, 420 (1968).
- [35] L. V. Al'tshuler and B. S. Chekin, *Proceed. of 1st All-Union Pulsed Pressures Symposium* **1**, 5 (1974).
- [36] L. V. Al'tshuler, N. Kalitkin, L. KuzŌmina, B. Chekin, *Zh. Eksp. Teor. Fiz* **72**, 317 (1977).
- [37] L. V. Al'tshuler, A. Bakanova, I. Dudoladov, E. Dynin, B. Chekin, *J. Appl. Mech. Techn. Phys.* **22**, 145 (1981).
- [38] L. V. Al'tshuler, R. F. Trunin, K. K. Krupnikov, N. Panov, *Physics-Uspekhi* **39**, 539 (1996).
- [39] L. V. Al'tshuler, S. B. Kormer, A. A. Bakanova, R. F. Trunin, *Sov. Phys. JETP* **11**, 573 (1960).
- [40] R. G. McQueen and S. P. Marsh, *Journal of Applied Physics* **31**, 1253 (1960).
- [41] R. G. McQueen, S. P. Marsh, J. W. Taylor, J. N. Fritz, W. J. Carter, *High velocity impact phenomena* **293**, 294 (1970).
- [42] I. C. Skidmore and E. Morris, *Thermodynamics of Nuclear Materials*, 173 (1962).
- [43] K. K. Krupnikov, A. A. Bakanova, M. I. Brazhnik, R. F. Trunin, *Soviet Physics Doklady* **8**, 205 (1963).
- [44] A. S. Balchan and G. R. Cowan, *J. Geophys. Res.* **71**, 3577 (1966).
- [45] C. E. Ragan III, *Physical Review A* **29**, 1391 (1984).
- [46] R. S. Hixson and J. N. Fritz, Technical report Los Alamos National Lab., NM (1991).
- [47] J. M. Brown, J. N. Fritz, R. S. Hixson, *J. Appl. Phys.* **88**, 5496 (2000).
- [48] R. F. Trunin, M. A. Podurets, G. V. Simakov, L. V. Popov, B. N. Moiseev, *Sov. Phys. JETP* **35**, 550 (1972).
- [49] R. F. Trunin, M. A. Podurets, L. V. Popov, V. N. Zubarev, A. A.

- Bakanova, *Zh. Eksp. Teor. Fiz* **102**, 1433 (1992).
- [50] R. F. Trunin, M. A. Podurets, B. N. Moiseev, G. V. Simakov, A. G. Sevast'yanov, *Zh. Eksp. Teor. Fiz* **103**, 2189 (1993).
- [51] R. F. Trunin, *Physics-Uspekhi* **37**, 1123 (1994).
- [52] R. Trunin, L. Gudarenko, M. Zhernokletov, G. Simakov, *RFNC, Sarov* (2001).
- [53] J.-P. Davis, M. D. Knudson, L. Shulenburg, S. D. Crockett, *Journal of Applied Physics* **120**(16), 165901 (2016).
- [54] J. Hawreliak, J. Winey, Y. Toyoda, M. Wallace, Y. Gupta, *Physical Review B* **107**(1), 014104 (2023).
- [55] S. M. Sharma *et al.*, *Phys. Rev. Lett.* **123**(4), 045702 (2019).
- [56] J. T. Larsen and S. M. Lane, *J. Quant. Spectrosc. Ra.* **51**(1), 179 (1994).
- [57] G. I. Kerley, *Sandia National Laboratory technical report SAND-93-0027* (1993).
- [58] S. Bratos, J.-C. Leicknam, M. Wulff, D. Khakhulin, *Journal of Synchrotron Radiation* **21**(1), 177 01 2014.
- [59] S. Singh *et al.*, *Journal of Synchrotron Radiation* **29**(4), 1033 6 2022.
- [60] A. Dewaele *et al.*, *Phys. Rev. Lett.* **97**, 215504 (2006).
- [61] L. S. Dubrovinsky, S. K. Saxena, F. Tutti, S. Rekh, T. LeBehan, *Phys. Rev. Lett.* **84**, 1720 (2000).
- [62] C. J. Wu *et al.*, *Physical Review B* (2023), in review.
- [63] L. Benedict, R. Kraus, S. Hamel, J. Belof, Technical report Lawrence Livermore National Lab.(LLNL), Livermore, CA (United States) (2022).
- [64] T. Sjostrom and S. Crockett, *Physical Review E* **97**(5), 053209 (2018).
- [65] A. M. Dziewonski and D. L. Anderson, *Phys. Earth Planet. Inter.* **25**(4), 297 (1981).
- [66] M. Akin and J. Nguyen, *Review of Scientific Instruments* **86**(4), 043903 (2015).
- [67] R. F. Smith *et al.*, *J. Appl. Phys.* **114**, 223507 (2013).
- [68] Y. B. Zel'Dovich and Y. P. Raizer, *Physics of shock waves and high-temperature hydrodynamic phenomena* (Courier Corporation,, 2002).
- [69] B. J. Jensen, *Los Alamos National Laboratory Report LA-14386* (2009).
- [70] W. Burgers, *Physica* **1**(7-12), 561 (1934).
- [71] H. K. Mao, P. M. Bell, J. W. Shaner, D. J. Steinberg, *J. Appl. Phys.* **49**(6), 3276 (1978).
- [72] W. Rong and G. Dunlop, *Acta Metallurgica* **32**(10), 1591 (1984).
- [73] D. Potter, *Journal of the Less Common Metals* **31**(2), 299 (1973).
- [74] N. R. Barton, D. E. Boyce, P. R. Dawson, *Textures and Microstructures* **35**, 372532 1 2002.
- [75] J. V. Bernier, M. P. Miller, D. E. Boyce, *Journal of Applied Crystallography* **39**(5), 697 Oct 2006.
- [76] S. Singh, D. E. Boyce, J. V. Bernier, N. R. Barton, *Journal of Applied Crystallography* **53**(5), 1299 Oct 2020.
- [77] A. Dewaele *et al.*, *Phys. Rev. B* **91**, 174105 May 2015.
- [78] H. Mao, W. A. Bassett, T. Takahashi, *Journal of Applied Physics* **38**(1), 272 (1967).
- [79] S. Labrosse, *Physics of the Earth and Planetary Interiors* **247**, 36 (2015), Transport Properties of the Earth's Core.
- [80] T. Sun, J. P. Brodholt, Y. Li, L. Vočadlo, *Physical Review B* **98**(22), 224301 (2018).
- [81] T. D. Cuong and A. D. Phan, *Vacuum* **185**, 110001 (2021).
- [82] Y. Sun, F. Zhang, M. I. Mendelev, R. M. Wentzcovitch, K.-M. Ho, *Proceedings of the National Academy of Sciences* **119**(2), e2113059119 (2022).
- [83] S. M. Stishov, *Soviet Physics Uspekhi* **17**(5), 625 may 1975.
- [84] O. Sorokhtin, G. Chilingar, N. Sorokhtin, In O. Sorokhtin, G. Chilingarian, N. Sorokhtin, editors, *Evolution of Earth and its Climate: Birth, Life and Death of Earth* volume 10 of *Developments in Earth and Environmental Sciences* pages 13–60. Elsevier (2011).
- [85] S. Labrosse, J.-P. Poirier, J.-L. Le Mouél, *Physics of the Earth and Planetary Interiors* **99**(1), 1 (1997).
- [86] F. D. Stacey and P. M. Davis, *Physics of the Earth* (Cambridge University Press,, 2008).
- [87] R. K. Bono, J. A. Tarduno, F. Nimmo, R. D. Cottrell, *Nature Geoscience* **12**(2), 143 Feb 2019.
- [88] Y. Zhang *et al.*, *Phys. Rev. Lett.* **125**, 078501 Aug 2020.
- [89] O. L. Anderson and A. Duba, *Journal of Geophysical Research: Solid Earth* **102**(B10), 22659 (1997).
- [90] K. K. M. Lee and R. Jeanloz, *Geophysical Research Letters* **30**(23) (2003).
- [91] A. Gando *et al.*, *Nature Geoscience* **4**(9), 647 Sep 2011.
- [92] J. A. Hawreliak *et al.*, *Physical Review B* **78**(22), 220101 (2008).

A structural study of hcp and liquid iron under shock compression up to 275 GPa

Saransh Singh, Richard Briggs, Martin G. Gorman, Lorin X. Benedict, Christine J. Wu, Amy L. Coleman, Federica Coppari, Amalia Fernandez-Pañella, Christopher McGuire, Melissa Sims, June K. Wicks, Jon H. Eggert, Dayne E. Fratanduono, Raymond F. Smith

Supplementary Materials

Supplementary Material Tables:

Table S1: Summary of data.

Table S2: Table of values used for estimating the latent heat of fusion.

Supplementary Material Figures:

Figure S1: hcp+liquid coexistence.

Figure S2: Pressure versus Temperature map for Fe.

Figure S3: Fit to Hugoniot data.

Figure S4: Laser focal spot spatial profile.

Figure S5: VISAR traces and Laser power profiles.

Figure S6: Calculated pole figures for the ambient bcc-phase

Figure S7: Calculated pole figures for the high pressure hcp-phase following the Burger's orientation relationship.

Figure S8: Calculated pole figures for the high pressure hcp-phase following the Mao-Bassett-Takahashi orientation relationship.

Figure S9: Calculated pole figures for the high pressure hcp-phase following the Potter orientation relationship.

Figure S10: Calculated pole figures for the high pressure hcp-phase following the Rong-Dunlop orientation relationship.

Figure S11: Simulated diffraction pattern for (a) ambient α -Fe and high-pressure ϵ -phase following the (b) Mao-Bassett-Takahashi, (c) Potter and (d) Rong-Dunlop orientation relationships. The equivalent results for the Burger's orientation relationship reported in Fig. 9.

Figure S12: X-ray Diffraction Lineouts (s19-C-122, s19-C-109, s19-C-129, s19-C-128).

Figure S13: X-ray Diffraction Lineouts (s19-C-121, s19-C-123, s19-C-124, s19-C-126).

Figure S14: X-ray Diffraction Lineouts (s19-C-125, s19-C-127, s19-C-088).

Table S1: Summary table of all shots taken in the experiment

Shot #	X-ray #	Pressure (GPa)	Phase	density (g/cm ³)
19-C-122	438	25(7)	hcp	9.208(5)
19-C-109	333	38(7)	bcc + hcp	8.036(3) 9.482(7)
19-C-129	496	33(6)	bcc + hcp	8.038(3) 9.242(3)
19-C-128	489	35(6)	hcp	9.301(4)
19-C-121	432	32(8)	bcc + hcp	8.023(3) 9.455(4)
19-C-123	448	57(7)	hcp	9.942(7)
19-C-124	454	92(7)	hcp	10.633(5)
19-C-126	468	93(8)	hcp	10.72(2)
19-C-125	462	96(7)	hcp	10.721(3)
19-C-127	474	103(7)	hcp	10.867(4)
19-C-088	182	210(13)	hcp	12.081(6)
19-C-068	037	258(8)	liquid	12.51 ± (0.3, 0.06)
19-C-117	393	275(9)	liquid	12.7 ± (0.35, 0.1)

S1. Latent Heat of Fusion

Following Ref. (19), the latent heat of fusion, ΔH_m is given by the expression

$$\Delta H_m = \frac{T_m \Delta V_m}{dT_m/dP}. \quad (4)$$

Here, T_m is the melt curve of iron, ΔV_m is the volume change due to melting and dT_m/dP is the Clapeyron slope. T_m and dT_m/dP were determined using the Simon fit melt curve in Ref. (20) given by

$$T_m = 5530 \left(\frac{P - 260}{293} + 1 \right)^{0.552}. \quad (5)$$

Here, T_m is the melt temperature in K and P is the pressure in GPa. The ΔV_m term is determined by the change in density of the last purely solid point at 241.5 GPa in Ref. (2), $\rho_{\text{start}}^{\text{sol}}$, and the density of the first purely liquid point at 258 GPa (shot 19-C-068) in our study, $\rho_{\text{end}}^{\text{liq}}$. As the pressure increases between these two data points, the ΔV from the volume difference between these points has contribution both from volume change due to melting, as well as volume change due to compression. The density change due to compression was estimated by using the theoretical value for the bulk modulus in the coexistence (14) using the equation

$$\Delta \rho_{\text{comp}} = \int_{P_{\text{start}}}^{P_{\text{end}}} \frac{\rho}{K} dP. \quad (6)$$

ΔV_m can be estimated using

$$\Delta V_m = \left(\frac{1}{\rho_{\text{end}}^{\text{liq}}} - \frac{1}{\rho_{\text{start}}^{\text{sol}} + \Delta \rho_{\text{comp}}} \right) \quad (7)$$

The table below shows the values and associated uncertainties used for estimating the latent heat. Assuming uncorrelated parameters, a final value of $\Delta H_m = 542(83)$ J/g is obtained.

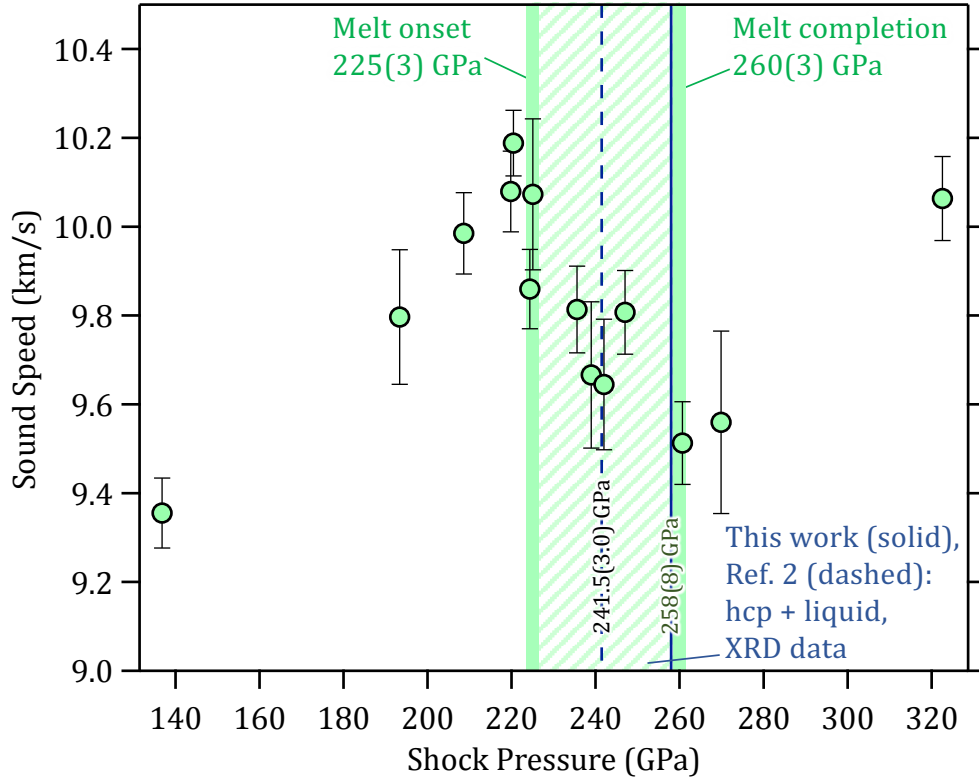


Figure S1: **Pressure versus sound speed.** Sound speed data from Nguyen and Holmes (1) (green symbols) as a function of shock pressure. While these data provide no direct structural information, changes in sound speed are interpreted as the onset and completion of melt, as indicated. In those experiments, the shock duration applied to mm-thick Fe samples was $\sim \mu\text{s}$. In contrast the combined XRD and laser shock compression experiments reported here use nanosecond shock compression of $21 \mu\text{m}$ thick samples. Our lowest pressure liquid only point is at $258(8)$ GPa (solid vertical line). This data combined with observations from a previous XRD study (2) places the completion of shock melt in the range $246.5(1.8)$ - $258(8)$ GPa. The hcp+liquid coexistence region from our data and an earlier XRD study (2) are consistent with onset (vertical dashed line) and completion of melt of $241.5(3.0)$ GPa and $258(8)$ GPa, respectively.

Table S2: **Table of values used for estimating the latent heat of fusion**

Parameter	Value (units)	Source
T_m (melting temperature)	5461 ± 530 K	Ref. (20)
dT_m/dP (Clapeyron slope of melt curve)	10.52 ± 1.21 K/GPa	Ref. (20)
$\rho_{\text{start}}^{\text{sol}}$ (density at melt start)	12.318 ± 0.078 g/cm ³	Hugoniot Fit in Fig. S3
$\rho_{\text{end}}^{\text{liq}}$ (density at melt end)	12.413 ± 0.077 g/cm ³	Hugoniot Fit in Fig. S3
P_{start} (Pressure at last purely hcp point)	225 ± 3.0 GPa	Ref. (2)
P_{end} (Pressure at first purely liquid point)	258 ± 8 GPa	This study
K_{T_m} (Isothermal bulk modulus in the solid-liquid coexistence)	linear between 936 - 978 GPa	Ref. (14)

S2. Sensitivity of XRD techniques to measuring small volumes of liquid/solid

Using XRD techniques our ability to constrain the extent of solid-liquid coexistence is limited by the ability to determine small volumes of liquid (melt onset) and solid (melt completion). For comparable volumes, scattering off liquid is more difficult to detect than a solid. Liquid diffraction is texture free (more powder like) and is broader in 2θ and lower in amplitude than scattering off a comparable volume of solid. In a mixed phase, if the signal from the liquid is below the threshold of detection then the analysis will show only compressed hcp as being present. In our transmission geometry shock compression in the mixed phase will result in a volume-integrated XRD pattern comprising of ambient-pressure bcc (ahead of the shock front), and compressed liquid+hcp behind (behind the shock front). Azimuthal averaging of the XRD pattern (see Figs. S12, S13, and S14) results in an overlap of three three

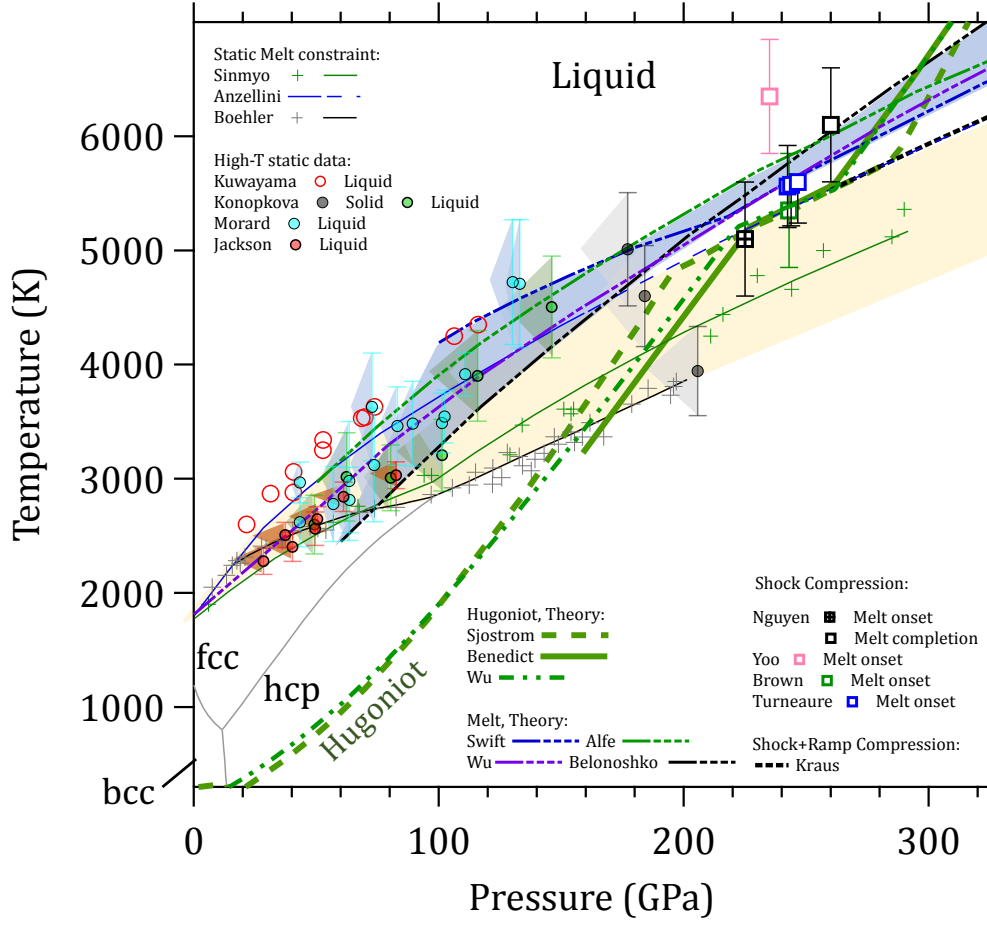


Figure S2: **Pressure versus Temperature.** Pressure-temperature phase map of Fe with three solid phases and a liquid phase. The melt line as constrained by static compression studies is bound by yellow shaded region (3–9). Bounds provided by theoretical calculations are shown by the blue shaded region (10–13). Three theoretical bounds on the Hugoniot are represented by the green curves (14–16). Determined pressure and estimated temperatures for previous sound speed measurements under shock compression (no direct lattice level observations) for the onset of shock melt (colored squares (1, 17, 18)) and full melt (white square (1)) are also shown, as well as the calculated melt onset temperature from a recent laser shock + XRD study (2).

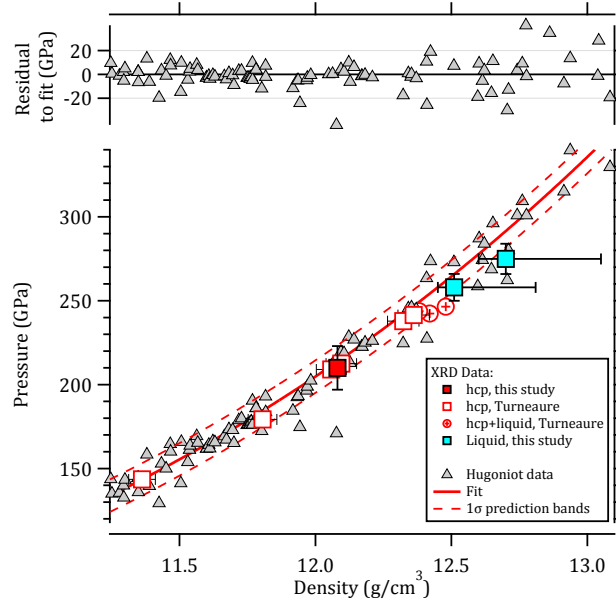
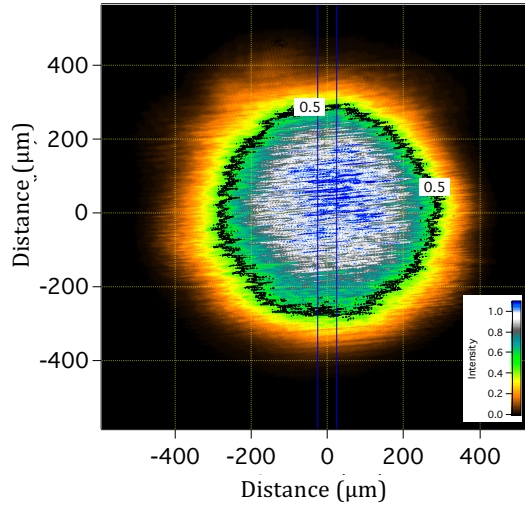


Figure S3: **Hugoniot Fit**. The red curve is based on a fit to previous Hugoniot data (grey triangles), and the dashed black lines are 1σ prediction bands which represents the bounds within which there is an expectation 68.3% of shock data points should fall within. The upper plots shows residuals to the fit. Cyan and green horizontal lines show pressures for onset and completion of melt from this study and from Ref. (1), respectively.

Equivalent Target Plane Image of 580 μm spot



Super-Gaussian Fit:

$$Int = \exp \left[-1 * \left(\text{abs} \left(\frac{x(\mu\text{m})}{x_0} \right) \right)^n \right]$$

$$x_0 = 310 \mu\text{m}, n=3.35$$

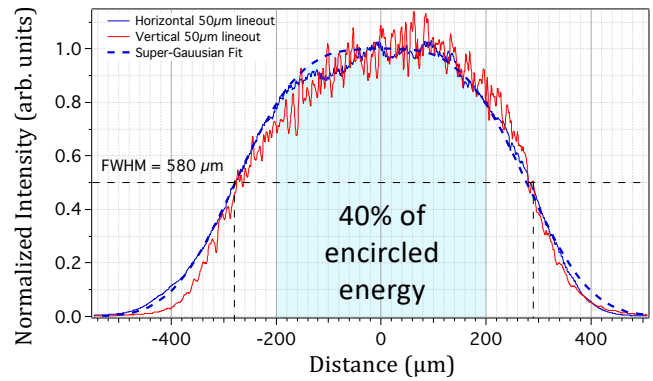


Figure S4: **DCS laser spot**. (left) Equivalent target plane image of DCS 580 μm diameter laser spot with a normalized intensity scale. The 0.5 intensity contour is highlighted. (right) Normalized intensity as a function of distance for 50 μm wide vertical (red) and horizontal (blue) lineouts from the image on the left (vertical lineout averaged between blue line in left image). The intensity lineouts are described by a super-Gaussian spatial profile (dashed blue curve), as indicated. Within this distribution 40% of the total energy is contained within the central 400- μm diameter spot (blue shaded region).

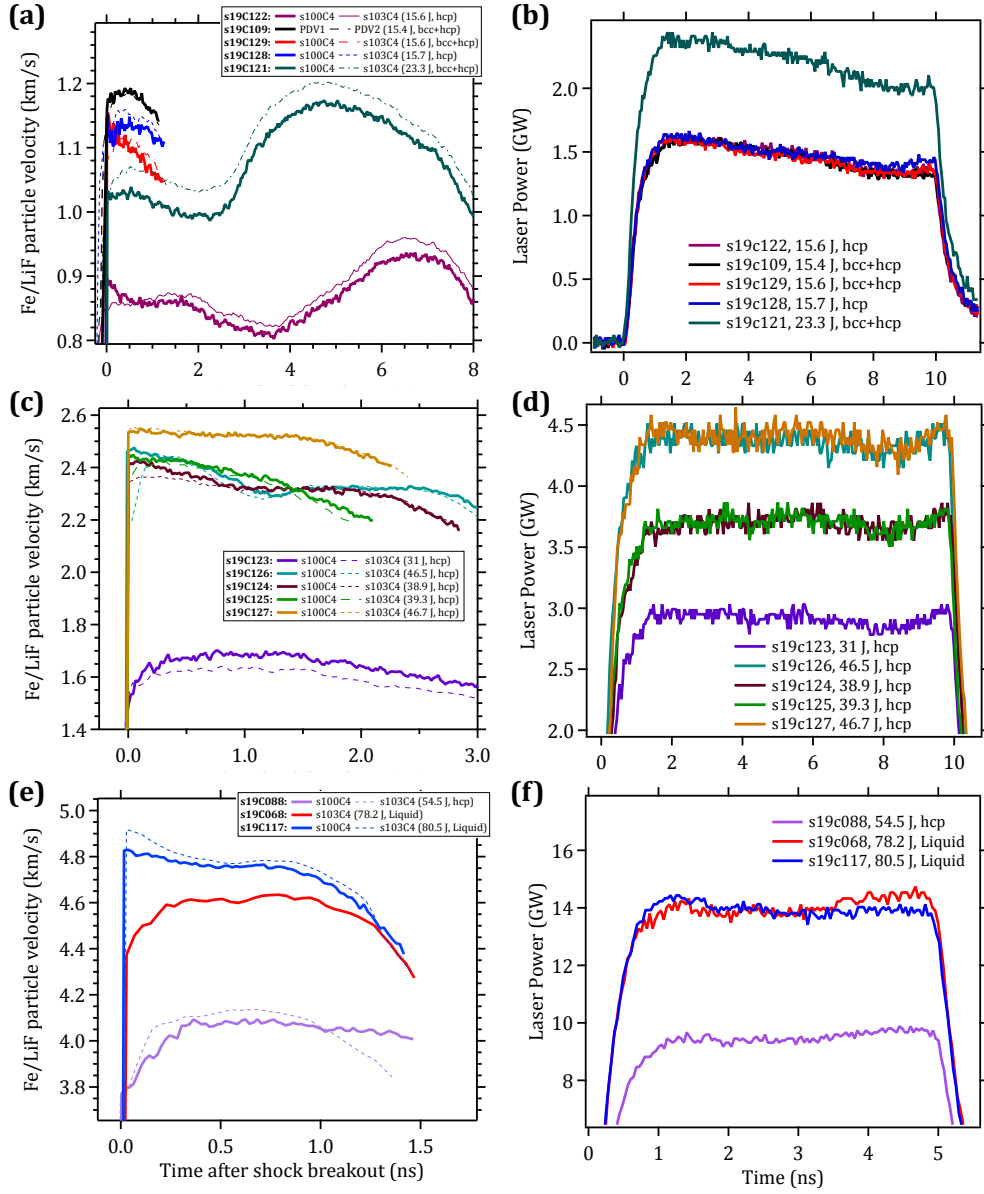


Figure S5: **Summary of Fe/LiF particle velocity traces (a), (c), (e), and the associated laser power versus time profiles (b), (d), (f).** The velocity traces were offset in time such that time=0 equates to the shock arrival time at the Fe/LiF interface. For some shots the point VISAR systems did not record usable data and instead a PDV VISAR record was used (23). The shot number, laser energy for each shot, as well as the measured phases are listed in the legend.

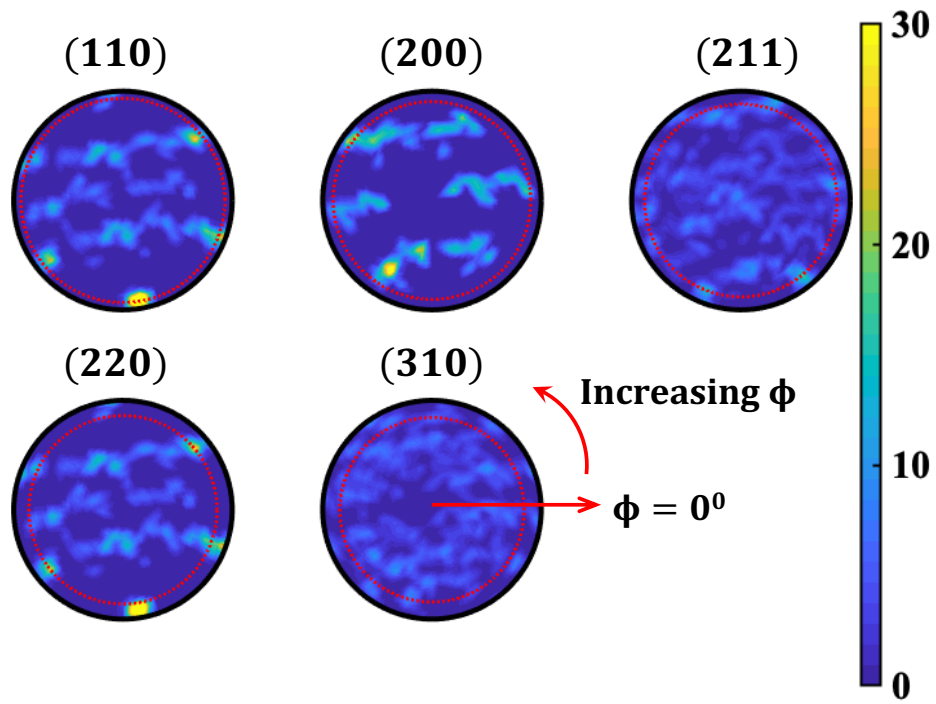


Figure S6: **Calculated pole figure for ambient α -Fe** Calculated pole figures for the initial texture of the ambient cubic Fe sample. The red circle shows the region of the $2\theta - \phi$ space which are measured with our diffraction geometry. Color bar units are m.r.d. (multiples of random distribution), where 1 is random texture and >1 is non random.

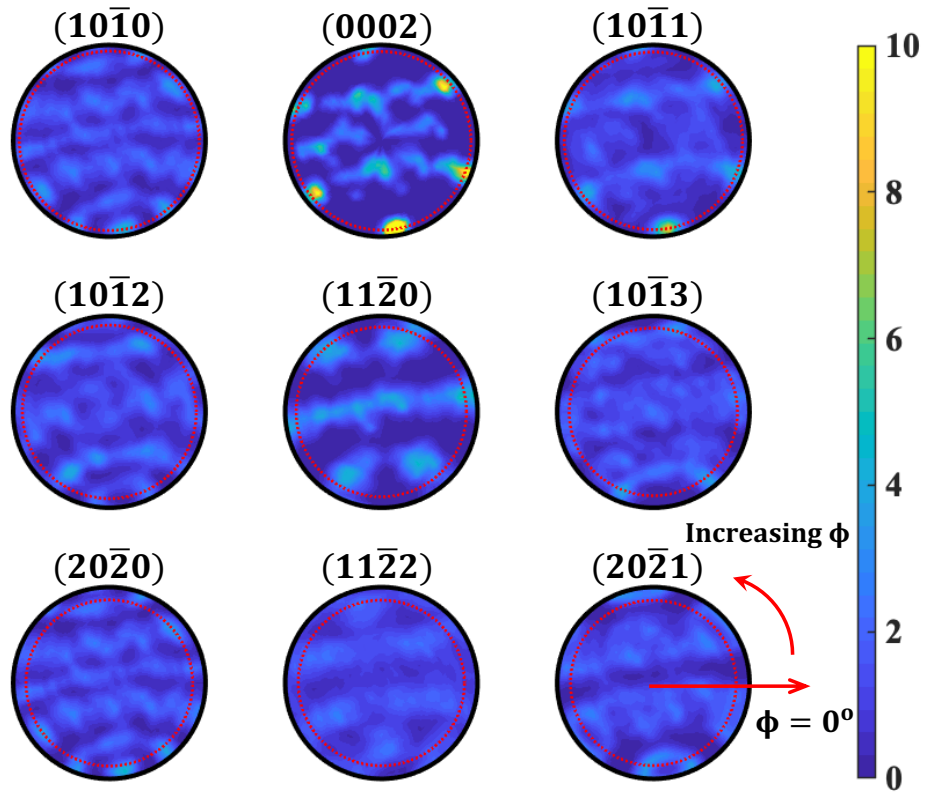


Figure S7: **Calculated pole figure for Burger's OR for high-pressure ϵ -Fe** Pole figures from applying the Burger's orientation relationship to the ambient sample texture shown in Fig. S6. The red circle shows the part of the $2\theta - \phi$ space probed in our diffraction measurements. Color bar units are m.r.d. (multiples of random distribution), where 1 is random texture and >1 is non random.

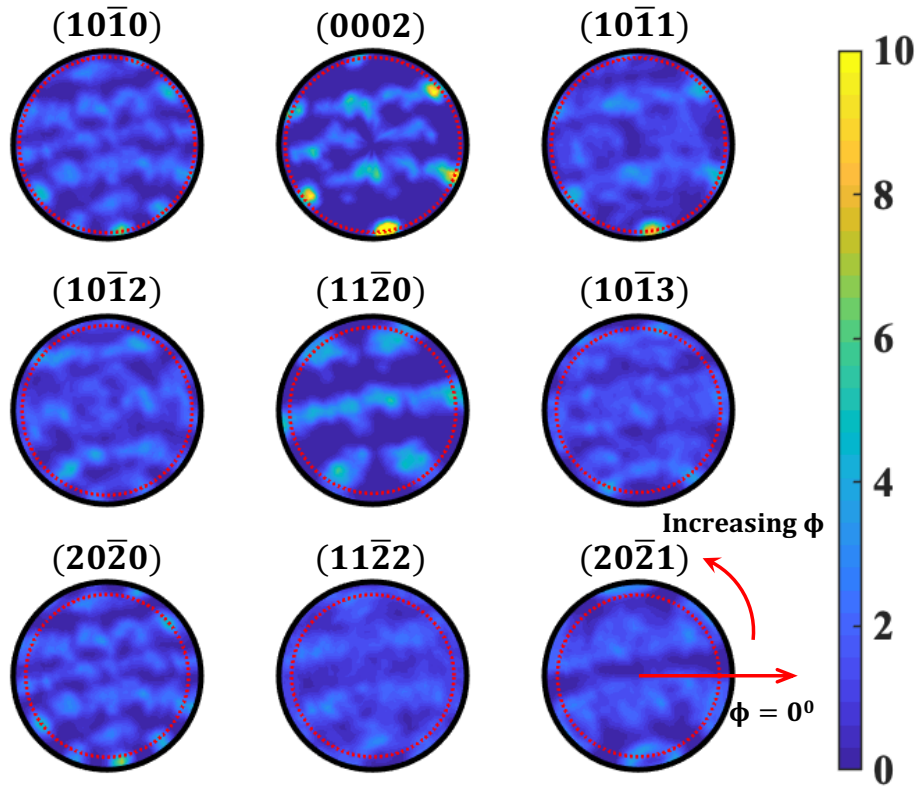


Figure S8: **Calculated pole figure for MBT OR for high-pressure ϵ -Fe** Pole figures from applying the Mao-Bassett-Takahashi orientation relationship to the ambient sample texture shown in Fig. S6. The red circle shows the part of the 2θ - ϕ space probed in our diffraction measurements. Color bar units are m.r.d. (multiples of random distribution), where 1 is random texture and >1 is non random.

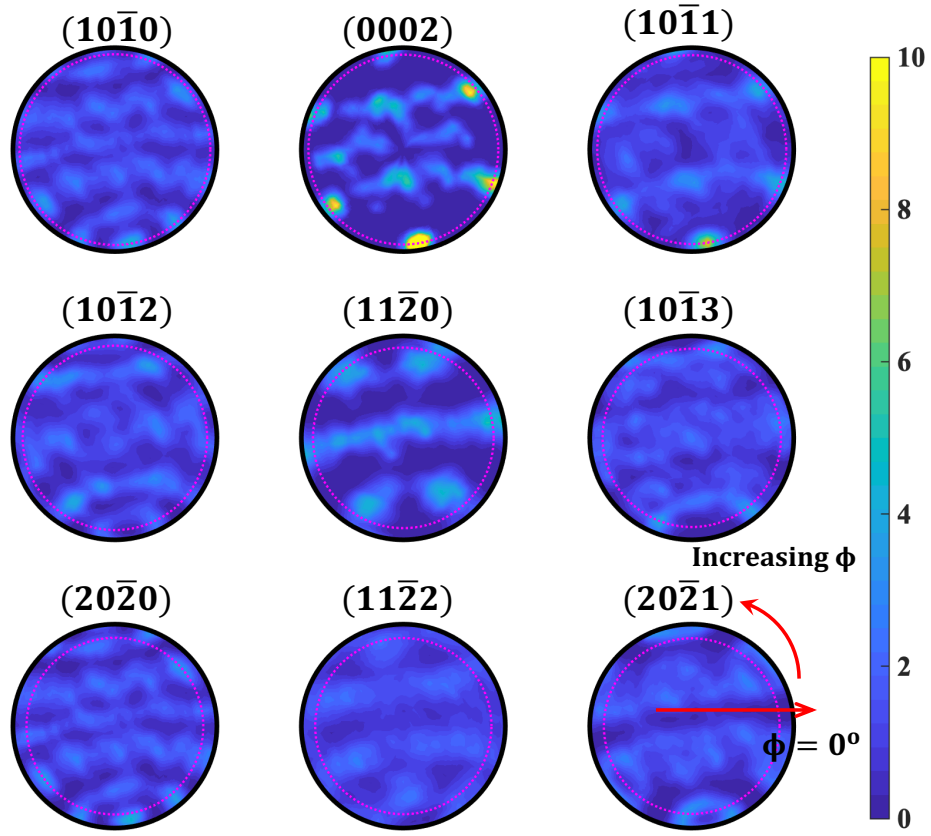


Figure S9: **Calculated pole figure for Potter's OR for high-pressure ϵ -Fe** Pole figures from applying the Potter orientation relationship to the ambient sample texture shown in Fig. S6. The red circle shows the part of the $2\theta - \phi$ space probed in our diffraction measurements. Color bar units are m.r.d. (multiples of random distribution), where 1 is random texture and >1 is non random.

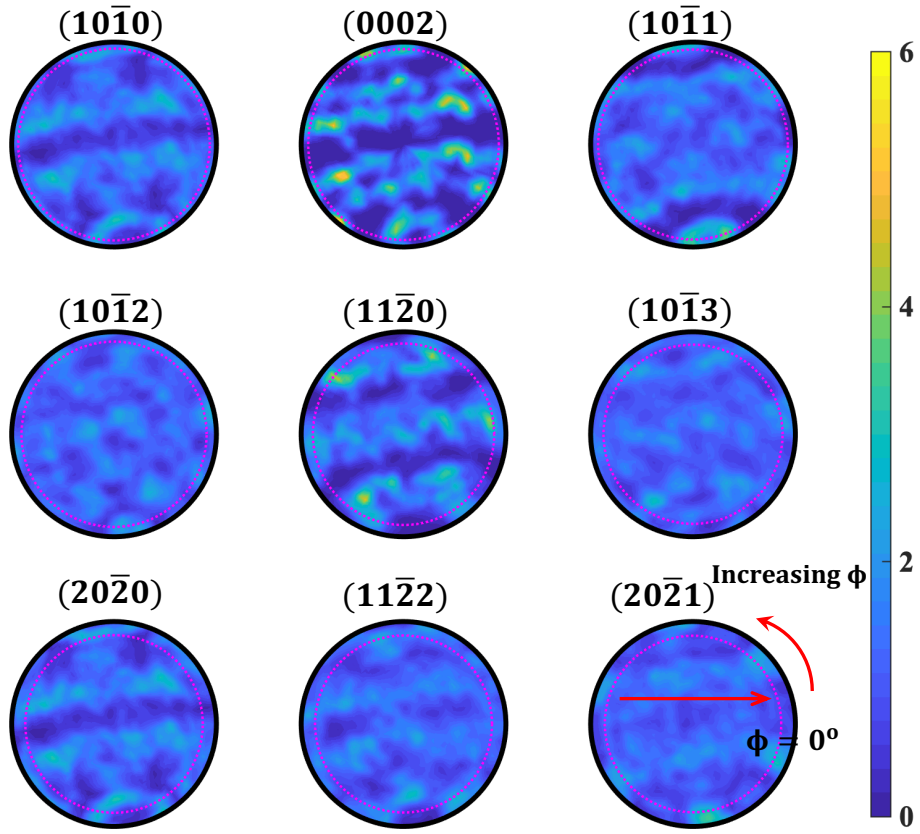


Figure S10: **Calculated pole figure for Rong-Dunlop OR for high-pressure ϵ -Fe** Pole figures from applying the Rong-Dunlop orientation relationship to ambient the sample texture shown in Fig. S6. The red circle shows the part of the 2θ - ϕ space probed in our diffraction measurements. Color bar units are m.r.d. (multiples of random distribution), where 1 is random texture and >1 is non random.

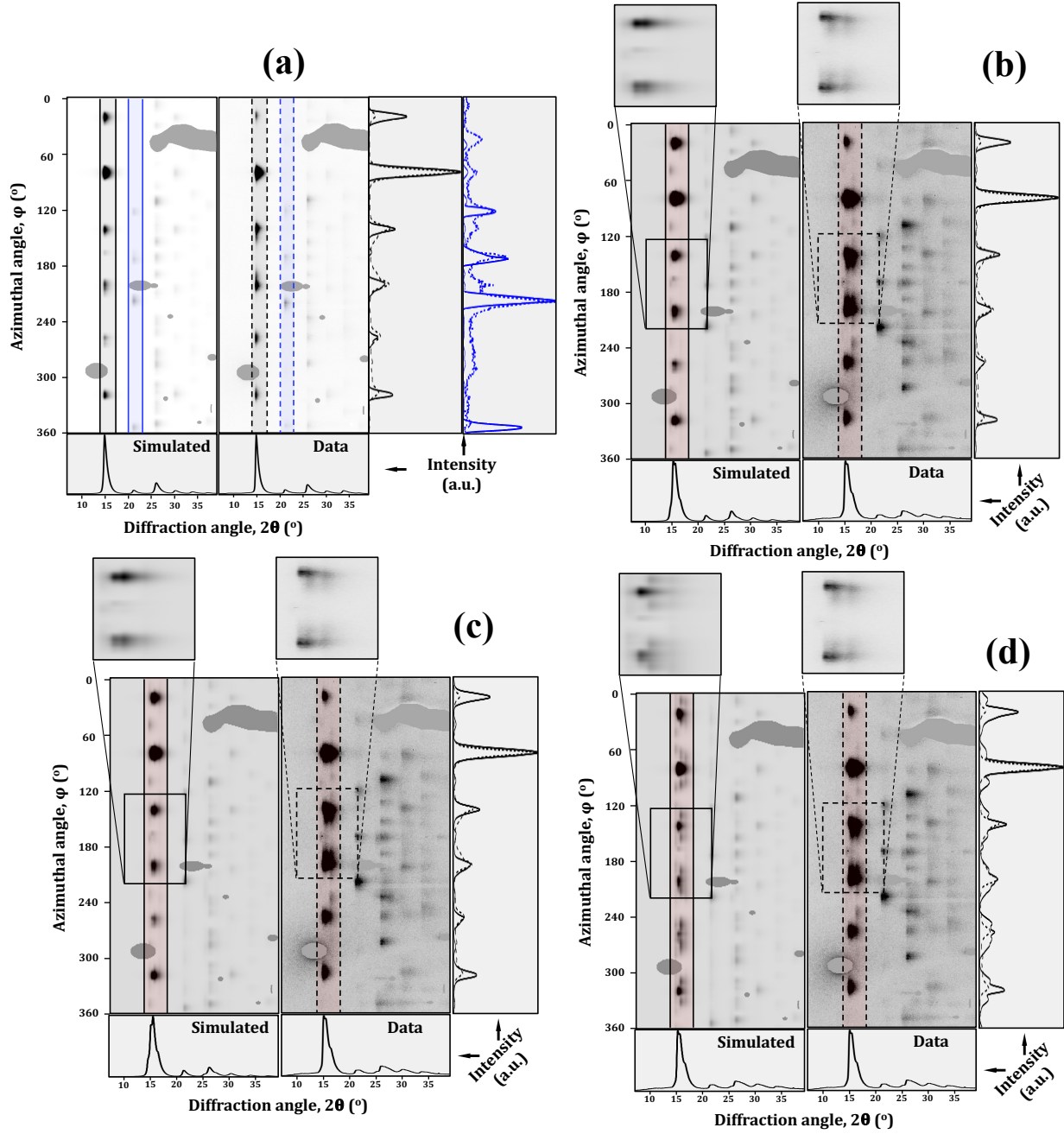


Figure S11: **Simulated diffraction patterns** Comparison of simulated diffraction signal with the experimental diffraction signal for (a) ambient α -Fe and high-pressure hcp phase following (b) Mao-Bassett-Takahashi (MBT) (c) Potter and (d) Rong-Dunlop ORs. The azimuthal lineout for the band between $14^\circ - 18^\circ$ diffraction angle is shown on the right for the simulated (solid) and experimental (dashed) signal. The azimuthally averaged lineout is shown at the bottom. The inset show presents a high-resolution view of a small section of the simulated and experimental data. We are not able to distinguish between the Burger's, MBT and Potter's OR based on our data. However, we are able to rule out the Rong-Dunlop OR.

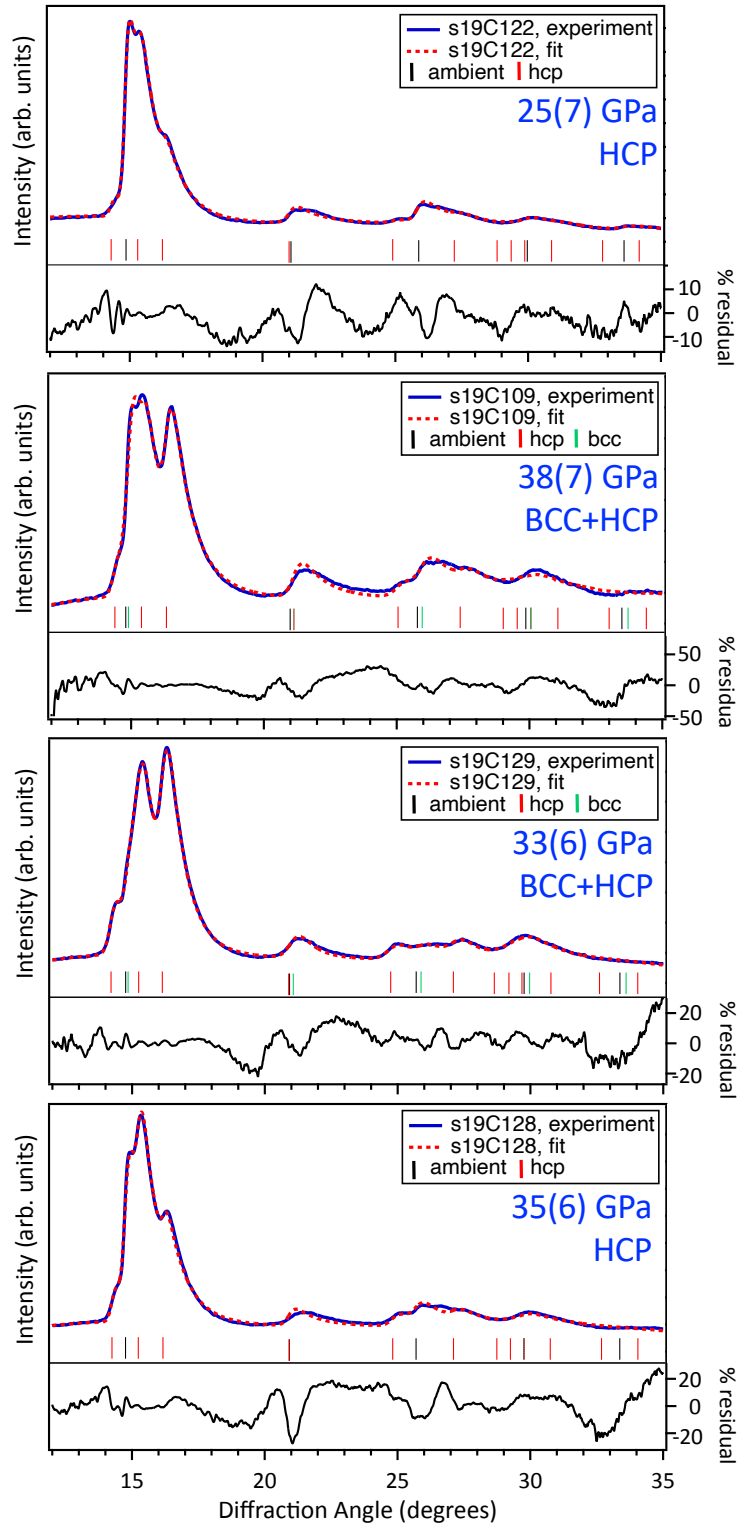


Figure S12: Azimuthally-integrated profiles for experiments s19C122, s19C109, s19C129, and s19C128 (blue) and fit using the HEXRD software (red dotted) (24). All profiles include a contribution from the unshocked-volume (ambient fcc-phase) ahead of the shock front (black ticks), and the shock-compressed fcc-phase (red ticks) and/or bcc-phase (green ticks). The % difference between the experimental profile and the fit is shown on the right hand axis.

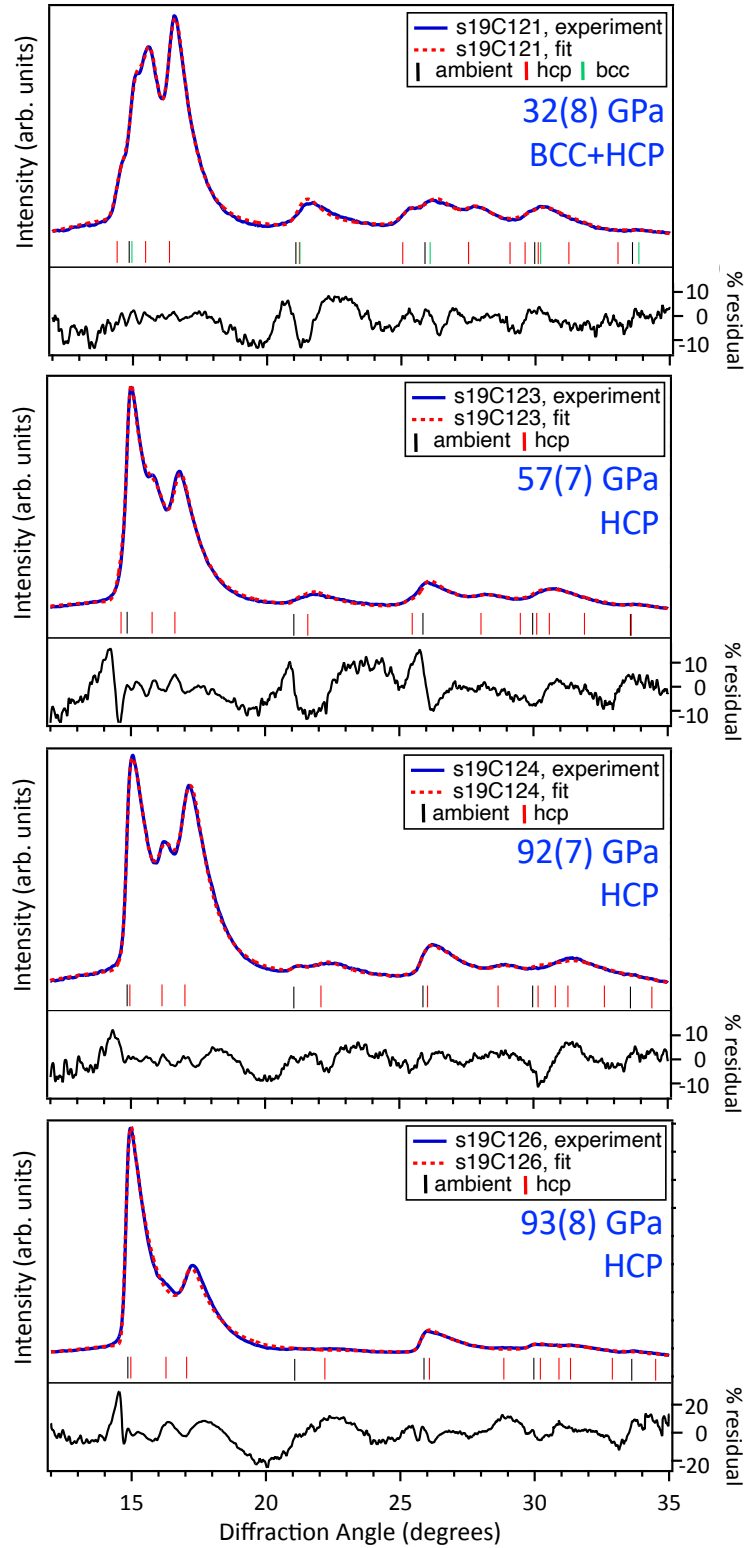


Figure S13: Azimuthally-integrated profiles for experiments s19C121, s19C123, s19C124, and s19C126 (blue) and fit using the HEXRD software (red dotted) (24). All profiles include a contribution from the unshocked-volume (ambient fcc-phase) ahead of the shock front (black ticks), and the shock-compressed fcc-phase (red ticks) and/or bcc-phase (green ticks). The % difference between the experimental profile and the fit is shown on the right hand axis.

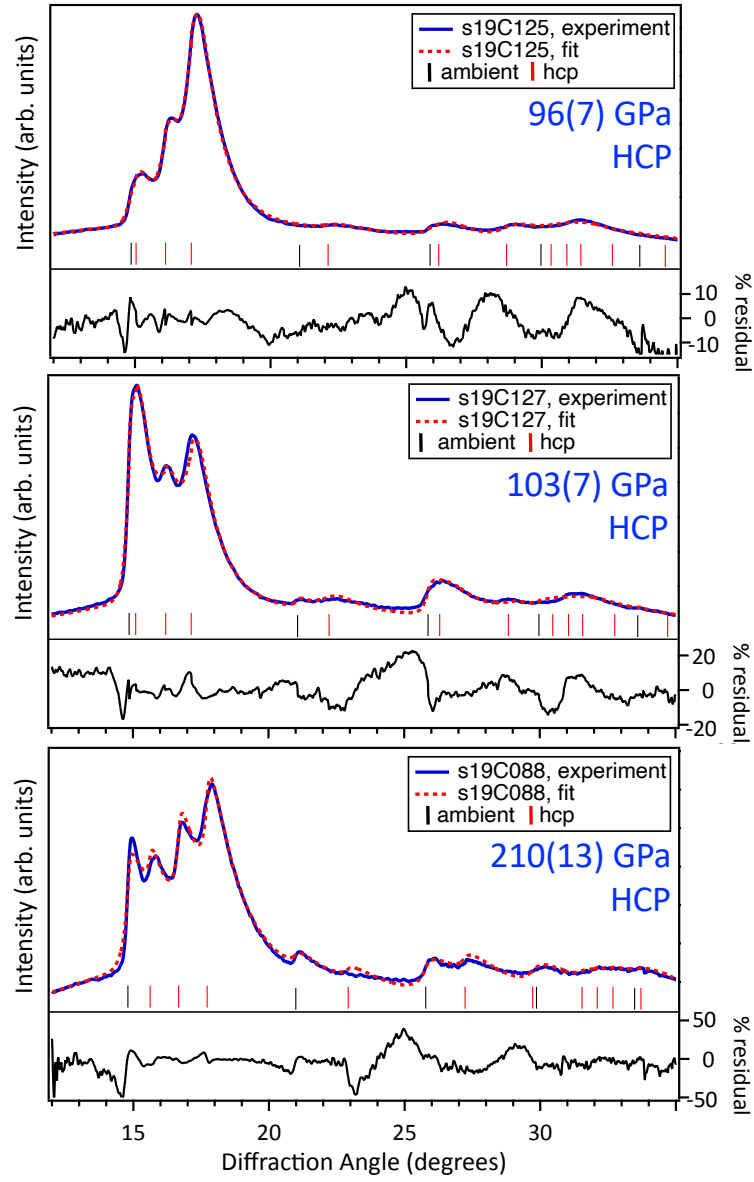


Figure S14: Azimuthally-integrated profiles for experiments s19C125, s19C127, and s19C088 (blue) and fit using the HEXRD software (red dotted) (24). All profiles include a contribution from the unshocked-volume (ambient fcc-phase) ahead of the shock front (black ticks), and the shock-compressed fcc-phase (red ticks) and/or bcc-phase (green ticks). The % difference between the experimental profile and the fit is shown on the right hand axis.

References

- [1] J. H. Nguyen, N. C. Holmes, Melting of iron at the physical conditions of the Earth's core, *Nature* 427 (2004) 339–342.
- [2] S. J. Turneaure, S. M. Sharma, Y. M. Gupta, Crystal structure and melting of fe shock compressed to 273 gpa: In situ x-ray diffraction, *Phys. Rev. Lett.* 125 (2020) 215702.
- [3] S. Anzellini, A. Dewaele, M. Mezouar, P. Loubeyre, G. Morard, Melting of iron at earth's inner core boundary based on fast x-ray diffraction, *Science* 340 (2013) 464–466.
- [4] R. Boehler, N. Von Bagen, A. Chopelas, Melting, thermal expansion, and phase transitions of iron at high pressures, *Journal of Geophysical Research: Solid Earth* 95 (B13) (1990) 21731–21736.
- [5] R. Boehler, Temperatures in the earth's core from melting-point measurements of iron at high static pressures, *Nature* 363 (6429) (1993) 534–536.
- [6] R. Sinmyo, K. Hirose, Y. Ohishi, Melting curve of iron to 290 GPa determined in a resistance-heated diamond-anvil cell, *Earth and Planetary Science Letters* 510 (2019) 45–52.
- [7] Z. Konôpková, W. Morgenroth, R. Husband, N. Giordano, A. Pakhomova, O. Gutowski, M. Wendt, K. Glazyrin, A. Ehnes, J. T. Delitz, et al., Laser heating system at the extreme conditions beamline, p02. 2, petra iii, *Journal of Synchrotron Radiation* 28 (6) (2021).
- [8] G. Morard, S. Boccato, A. D. Rosa, S. Anzellini, F. Miozzi, L. Henry, G. Garbarino, M. Mezouar, M. Harmand, F. Guyot, et al., Solving controversies on the iron phase diagram under high pressure, *Geophysical Research Letters* 45 (20) (2018) 11–074.
- [9] J. M. Jackson, W. Sturhahn, M. Lerche, J. Zhao, T. S. Toellner, E. E. Alp, S. V. Sinogeikin, J. D. Bass, C. A. Murphy, J. K. Wicks, Melting of compressed iron by monitoring atomic dynamics, *Earth and Planetary Science Letters* 362 (2013) 143–150.
- [10] D. Alfe, Temperature of the inner-core boundary of the earth: Melting of iron at high pressure from first-principles coexistence simulations, *Physical Review B* 79 (6) (2009) 060101.
- [11] D. C. Swift, T. Lockard, R. F. Smith, C. J. Wu, L. X. Benedict, High pressure melt curve of iron from atom-in-jellium calculations, *Physical Review Research* 2 (2) (2020) 023034.
- [12] A. B. Belonoshko, R. Ahuja, B. Johansson, Quasi-ab initio molecular dynamic study of fe melting, *Physical Review Letters* 84 (16) (2000) 3638.
- [13] Y. Wu, D. Wang, Y. Huang, Melting of iron at the earth's core conditions by molecular dynamics simulation, *AIP Advances* 1 (3) (2011) 032122.
- [14] C. J. Wu, L. X. Benedict, P. C. Myint, S. Hamel, C. J. Prisdrey, J. R. Leek, A wide-ranged multiphase equation of state for iron, and model variations addressing uncertainties in high-pressure melting, *Physical Review B* in review (2023).
- [15] T. Sjostrom, S. Crockett, Quantum molecular dynamics of warm dense iron and a five-phase equation of state, *Physical Review E* 97 (5) (2018) 053209.
- [16] L. Benedict, R. Kraus, S. Hamel, J. Belof, A limited-ranged two-phase iron equation of state model, Tech. rep., Lawrence Livermore National Lab.(LLNL), Livermore, CA (United States) (2022).
- [17] J. M. Brown, R. G. McQueen, Phase transitions, Grüneisen parameter, and elasticity for shocked iron between 77 GPa and 400 GPa, *J. Geophys. Res.* 91 (1986) 7485.
- [18] C. Yoo, N. Holmes, M. Ross, D. Webb, C. Pike, Shock temperatures and melting of iron at earth core conditions, *Physical Review Letters* 70 (25) (1993) 3931.
- [19] O. L. Anderson, A. Duba, Experimental melting curve of iron revisited, *Journal of Geophysical Research: Solid Earth* 102 (B10) (1997) 22659–22669.
- [20] R. G. Kraus, R. J. Hemley, S. J. Ali, J. L. Belof, L. X. Benedict, J. Bernier, D. Braun, R. Cohen, G. W. Collins, F. Coppari, et al., Measuring the melting curve of iron at super-earth core conditions, *Science* 375 (6577) (2022) 202–205.
- [21] P. Renganathan, S. M. Sharma, S. J. Turneaure, Y. M. Gupta, Real-time (nanoseconds) determination of liquid phase growth during shock-induced melting, *Science Advances* 9 (8) (2023) eade5745.
- [22] S. J. Turneaure, S. M. Sharma, Y. M. Gupta, Crystal structure and melting of fe shock compressed to 273 gpa: In situ x-ray diffraction, *Phys. Rev. Lett.* 125 (2020) 215702.
- [23] D. H. Dolan, Foundations of visar analysis., Tech. rep., Sandia National Laboratories (SNL), Albuquerque, NM, and Livermore, CA (2006).
- [24] Hexrd, <https://github.com/HEXRD/hexrd>, LLNL-CODE-819716.